IPP-Report

Max-Planck-Institut für Plasmaphysik

Bailey Curzadd

Topology optimization of bimaterial W/Cu structures for plasma-facing component applications

IPP 2019-09
April 2019

Master Thesis in Mechanical Engineering at
Technische Universität München

Topology optimization of bimaterial W/Cu structures for plasma-facing component applications

presented by

Bailey Curzadd

May 30, 2018

First Promoter: Prof. Dr. Rudolf Neu

Supervisor: Alexander von Müller

Abstract

Tungsten has established itself as the most suitable plasma-facing material for long-term operation in future magnetic-confinement fusion devices. However, the properties of pure tungsten make it a poor structural material and complicate the manufacturing of complex components. Recent advances in additive-manufacturing (AM) technology have begun to make the production of tungsten components with complex geometry more feasible. The design freedom afforded by AM could be leveraged to produce more resilient plasma-facing components (PFCs).

To this end, a methodology to optimize the material distribution of composite PFCs was developed to reduce the maximum thermal stress caused by high heat fluxes. This methodology is primarily intended to be used with copper-infiltrated AM tungsten (W_{AM}/Cu) structures. The C++ implementation of this methodology was used to optimize a typical PFC configuration for numerous test cases. Stress reductions of approximately 50 - 85% were observed under nominal load conditions. Off-nominal conditions produce higher stresses, but the stress maximum generally remains an improvement over traditional designs. The resulting optimized structures are composed of a spatially heterogeneous distribution of tungsten and copper comprising a broad range of composite mixtures. In order to estimate the material properties of these composites for all compositions at relevant temperatures, a tool was developed to numerically determine the thermomechanical properties of composites with cuboid unit cells, and was tested on two example AM microstructures.

Using numerically optimized W_{AM}/Cu composite structures, sample components were modelled in CAD software, analyzed, and compared to traditional PFC designs. Simulated stress levels in the topology-optimized PFCs designed with this technique are significantly lower than in traditional designs. The methodology developed in this work may be a valuable tool for the design of reliable, economical components for plasma-facing applications.

Acknowledgements

I would like to thank my advisor Alexander von Müller for his support and encouragement throughout this project. I hope my work may eventually help him reach his own research goals. I am also thankful to Professor Rudolf Neu for his advice and the opportunity to perform the work for this thesis in his research group.

Further, I am ever grateful for the support of my family: my parents, who inspired me to pursue the crazy plans I regularly dream up; my wife Danielle, who has kindly humored those crazy plans and followed me around the world to see them through; and my grandfather, for being a constant reminder of the engineer I strive to be.

Contents

Chapter 1

Introduction

1.1 Background

Harnessing atomic fusion for energy production is a common theme in futuristic science fiction. However, this goal is closer than one might believe; a considerable amount of research since the mid-20$^{\text{th}}$ century has focused on making fusion energy a reality. One of the most well-studied concepts for future fusion power plants employs a reactor, the *tokamak*, that confines a high-temperature hydrogen plasma – up to 150 million °C – in a powerful toroidal magnetic field. Two isotopes of hydrogen, deuterium and tritium, fuse in the core of the plasma, and the released energy is exhausted through the wall of the reactor to be used for electricity production.

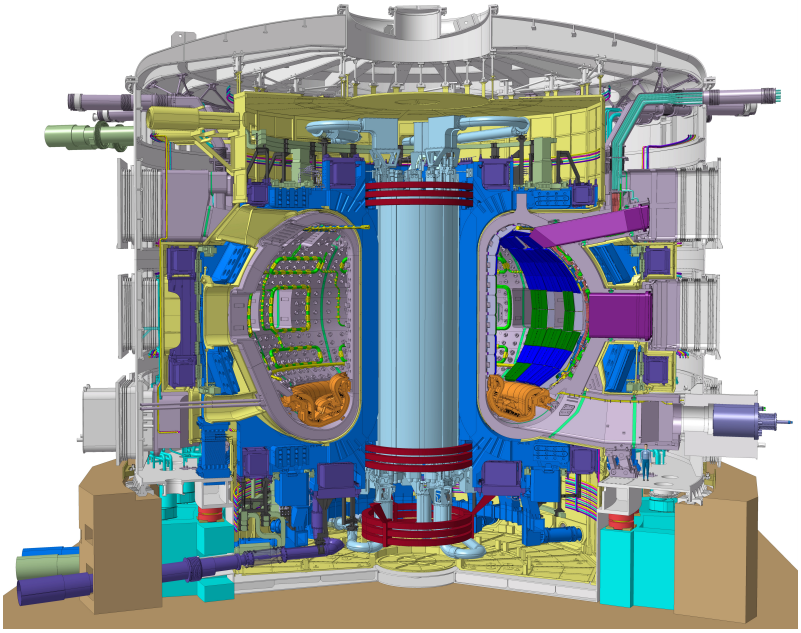

FIGURE 1.1: A cutaway drawing of the ITER tokamak [1].

These reactors have yet to be used to produce electricity, though, since no historical or contemporary reactor has yielded more power than is required to heat the plasma to the extreme temperatures required for fusion to take place. Researchers developing the next generation of tokamaks hope to change this precedent. A large consortium of countries are cooperating to create the world's first tokamak with net energy gain: *ITER* [1]. This massive device, illustrated in Figure 1.1, is currently under construction in Cadarache, France. ITER is an experimental platform, meant as a test bed for new technologies to pave the way for economical fusion energy production.

Magnetic-confinement fusion is one of the most complex technical problems mankind has attempted to solve, and many challenges remain. The challenge addressed in this work is the design of the plasma-facing components (PFCs) that line the vessel wall. These components protect the structure of the reactor from the heat and radiation released during fusion, and are exposed to high heat fluxes during operation. The thermal loads are most extreme at the reactor's divertor (see Figure 1.2), located at the bottom of the vacuum vessel. The nominal steady-state heat flux expected at the ITER divertor is 10 MW/m^2, with transient heat loads potentially as high as 20 MW/m^2 [2]. As will be discussed, high-heat-flux (HHF) loading poses many problems for the design of the PFCs in this region.

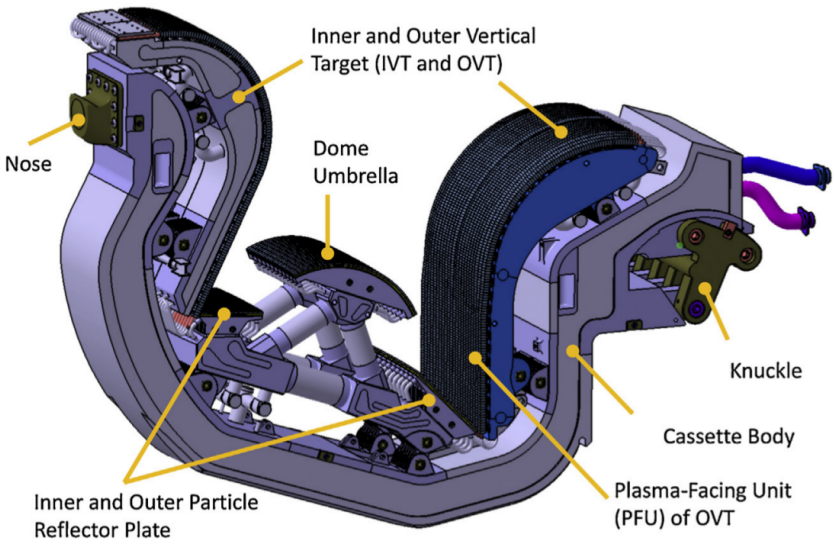

FIGURE 1.2: The main components of the ITER tungsten divertor [2].

1.2 Research aims and outline

The principal goal of this work is to develop a methodology to help design more robust composite PFCs by reducing the thermal stresses that develop under HHF loading. This methodology is primarily meant to be employed for components that will be fabricated using additive manufacturing. Central to this methodology is a toolset with which PFC designs can be optimized. The foundation of this toolset consists of two programs:

- *homog3d* – Calculates the effective 3D thermomechanical properties of composite microstructures with cuboid unit cells by homogenization.
- *TopOpt* – Determines the optimal material distribution to reduce stress in components exposed to steady-state high heat fluxes by topology optimization.

Although the primary purpose is to develop a toolset capable of design optimization for PFCs in any configuration, the process is demonstrated throughout with concrete examples based on well-known microstructures and a simplified ITER-like PFC geometry.

After a review of contemporary research on the topic and the current state of applicable technology in Chapter 2, W/Cu composite microstructures are investigated in Chapter 3. The process to calculate their effective properties by homogenization is explained, and the material models produced in this manner by the *homog3d* code are presented. Chapter 4 subsequently details the proposed method to optimize PFCs, discusses its implementation in *TopOpt*, and presents the results for test cases using the microstructures examined in the preceding chapter. Finally, use of the toolset to create manufacturable components is demonstrated and its effectiveness verified in Chapter 5 using two sample designs. Chapter 6 discusses the results and suggestions for future work. An overview of the finite-element formulation used in both codes and relevant notation is provided in Appendix A.

Chapter 2

Review of current research and technology

2.1 Plasma-facing materials

The interior of a fusion reactor is an extreme environment; in-vessel components like the divertor and first wall are exposed directly to the fusion plasma. Components in these regions are subjected to bombardment by energetic particles, which results in intense heat loads. This places demanding, sometimes contradictory requirements on the armor materials lining the reactor. Assessment of potential plasma-facing materials (PFMs) for fusion reactors has been performed by many authors (see [3, 4, 5], for example). The following lists key selection criteria for PFMs discussed in the literature:

- *Low erosion* – Bombardment with energetic particles sputters the surface of components, causing erosion and releasing impurities into the plasma. The rate of erosion must be limited to ensure components have an economical lifespan and to maintain reactor performance.
- *Low atomic number (Z)* – Impurities in the core plasma reduce reactor performance. This effect is stronger for high-Z elements: incomplete ionization increases radiative cooling, reducing plasma temperature, and the large positive charge of their nucleus displaces greater amounts of hydrogen fuel.
- *Low tritium retention* – Deposition of this radioactive hydrogen isotope in the reactor wall is a safety hazard and complicates the disposal or recycling of PFCs. Additionally, removal of tritium from the plasma precludes its use as fuel in the fusion reaction, which negatively impacts reactor performance and economics.
- *Resistance to high temperatures* – Heat is exhausted through the reactor wall at very high power densities. This thermal load results in high temperatures, especially at the plasma-facing surface. PFMs must retain their properties at these high temperatures.

- *Low vapor pressure* – In addition to erosion, material loss occurs in vacuum by sublimation at high temperatures. Materials with a high vapor pressure sublime at higher rates.

- *Structural integrity* – The extreme temperature gradients resulting from high heat fluxes produce substantial thermal stress. These thermal stresses must not cause material failure.

In addition to the charged particles that erode the surface of plasma-facing material, reactor components receive high doses of neutron radiation over their operational lives. Neutron bombardment causes microstructural defects and transmutations that induce changes such as swelling, creep, and altered properties [6]. The combination of extreme heat flux and neutron radiation makes the design of PFCs a challenging issue.

Few materials have the necessary properties to sustain direct exposure to the fusion plasma for extended periods of operation, and no one material meets all criteria for the "ideal" PFM. Only three armor materials were considered for use in ITER: carbon fiber reinforced carbon (CFC), beryllium (Be), and tungsten (W), each of which has its share of positive and negative features.

CFC has good thermal conductivity, high strength, and, unlike metals, does not melt. These properties make it fitting for use in HHF applications. However, despite its advantageous thermal and mechanical properties, carbon suffers from high rates of hydrogen isotope co-deposition and chemical erosion by formation of hydrocarbons.

The low atomic number of beryllium was vital to its selection as the armor material for the ITER blanket. The blanket comprises roughly 80% of the plasma-exposed surface in the reactor; an abundance of sputtered high-Z impurity atoms from such a large area and their proximity to the plasma core would have a significant impact on reactor performance. However, beryllium is not suitable for all regions of the reactor, especially the divertor: its erosion resistance is inferior to that of tungsten, and its resistance to thermal fatigue and shock is poor.

Tungsten has the highest melting point of all metals, excellent high-temperature properties, and a low vapor pressure. Most importantly, tungsten retains a minimal tritium inventory, and has the lowest sputtering yield among candidate materials, which makes it the most suitable divertor armor and a promising material for long-term operation in future reactors. The poor plasma-compatibility of tungsten is its main disadvantage. Recent research has focused heavily on understanding and improving the performance of tungsten as a PFM (see [7, 8, 9, 10, 11], for example).

Because the requirements for PFMs are governed chiefly by plasma interaction, most choices sacrifice structural performance. PFMs are therefore attached to a heat sink, which serves as a structural foundation and provides cooling. The two candidate heat-sink materials for ITER are both copper alloys: CuCrZr, a precipitation-hardened alloy, and CuAl25, an oxide dispersion-strengthened alloy. These copper alloys have a very narrow window of operational temperatures without reinforcement due to radiation-induced embrittlement at low temperatures (<150°C), and softening and creep at high-temperatures (>300-400°C) [12, 13].

2.2 W/Cu plasma-facing components

Clearly, no one material meets all of the requirements for structural integrity and interaction with the fusion plasma on its own. To be robust and economical, PFCs must thus make use of multiple materials. Current research focuses heavily on designing components that combine the advantages of tungsten armor and copper-alloy heat sinks (typically CuCrZr). Multi-material PFCs are generally fabricated according to one of the following two paradigms.

Monoblock designs join numerous tiles of armor material (the monoblocks) to a copper-alloy cooling tube (Figure 2.1).

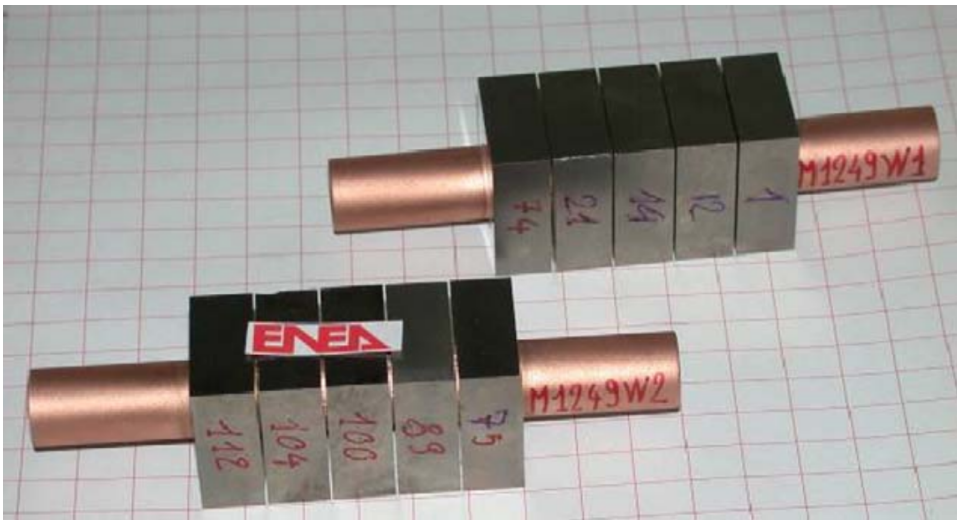

FIGURE 2.1: PFC Mockups of a monoblock design [14].

The simple geometry of an individual monoblock makes fabrication straightforward, an important consideration for a difficult-to-work material like tungsten. However, this configuration confines a high-thermal-expansion material (the Cu-alloy tube) within a stiff, low-thermal-expansion material (the W

monoblock). Upon heating, this leads to high thermal stresses. Failure often occurs at the cooling tube interface [15] or due to the propogation of radial cracks between the cooling tube and plasma-facing surface during the cooling phase of a thermal cycle [16, 17]. These issues are aggravated by the brittleness of tungsten near the cooling channel, where the temperature is below tungsten's ductile-to-brittle transition temperature (DBTT).

An alternative to tungsten monoblock designs is the "flat-tile" design: a monolithic copper-alloy heat sink shielded by castellated tiles of tungsten armor (Figure 2.2).

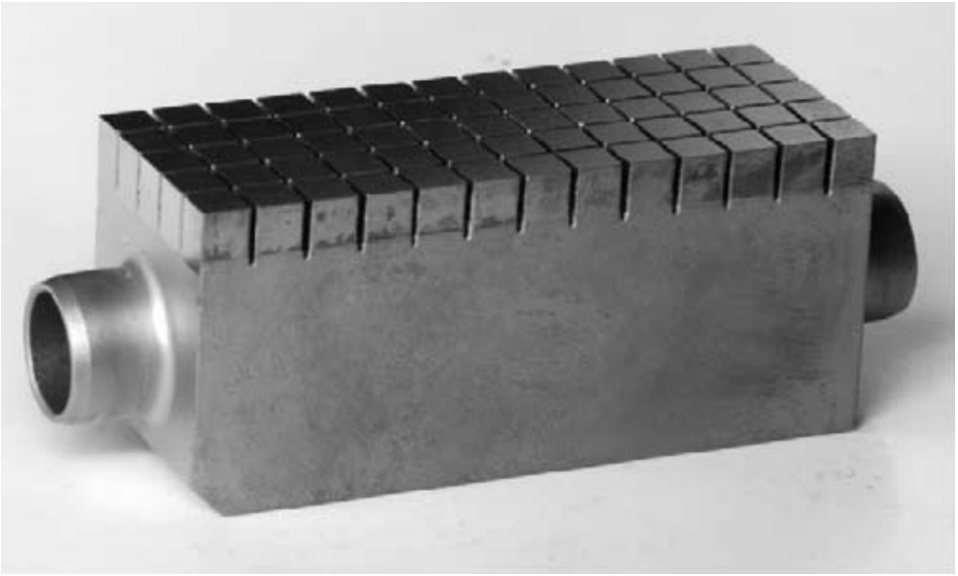

FIGURE 2.2: Tungsten-armored flat-tile mockup [10].

The flat-tile design combines the advantages of tungsten as plasma-facing armor with the excellent thermal conductivity and superior low-temperature mechanical properties of copper alloys. Despite the theoretical advantage of this arrangement, performance is limited by the lack of a robust bond at the heat-sink/armor interface. Failure of a flat-tile design generally results from high stresses at the free edges of the interface. This effect is especially detrimental for a combination of tungsten and copper, due to their vastly different thermomechanical properties. You and Bolt developed an analytical description of the stress singularities that develop at the free edges of bimaterial joints in PFCs. Their model indicates that, among the material combinations considered, a W/Cu interface experiences the most pronounced stress singularity [18].

The performance of both monoblock and flat-tile designs is limited by failure at the W/Cu interface. The stresses that lead to failure are the result of tungsten's and copper's dissimilar material properties, especially the large

difference in thermal expansion. Mitigating the effects of dissimilar thermomechanical properties requires the use of composites and stress-reducing design features.

2.2.1 W/Cu composite materials

As in many other demanding fields, composites are a promising solution to improve and tailor the properties of materials for components exposed to the extreme conditions in fusion reactors. Much recent work has focused on developing these advanced materials and complementary design techniques for PFCs exposed to HHF loading.

The composites of interest for PFC applications generally take the form of a copper-alloy matrix with tungsten reinforcement, either as particles or fibers. A review of CuCrZr-matrix composites for divertor heat sinks with SiC-fiber, W-wire, and W-particle reinforcements is provided by You in [19]. The author remarks that such composites increase the strength of copper-alloy heat sinks in general and mitigate thermal strain mismatch between the heat sink and tungsten armor. Von Müller et al. produced W-particle- and W-fiber-reinforced materials by Cu-melt infiltration for PFC heat sinks [20]. You et al. investigated the properties of melt-infiltrated porous skeletons of sintered tungsten in [21]. The thermomechanical behavior and failure mechanisms of these composites were investigated by Zivelonghi et al. [22] and Zivelonghi and You [23], and Tejado et al. characterized the dependence of their material properties on copper content and temperature [24, 25]. The intended use of these composites is the creation of a graded interlayer to reduce stress at the heat-sink/armor interface. This is discussed further in the following section.

Powder-based composites can also be processed by additive manufacturing. Yan et al. characterized samples produced from W-(Ni)-Cu powder mixtures by Selective Laser Melting [26]. Although this technique allows freeform design of part geometry, it is limited to producing components with one homogeneous material. Local tailoring of properties within the additively manufactured body is not possible.

2.2.2 Stress-reducing mechanisms

In order to make full use of the advantageous properties of composites, component designs must tailor the material to the needs of the application. A classic example is the alignment of fiber orientation to the loads applied to a fiber-reinforced composite. A number of design techniques have been proposed to minimize thermal stress in W/Cu PFCs.

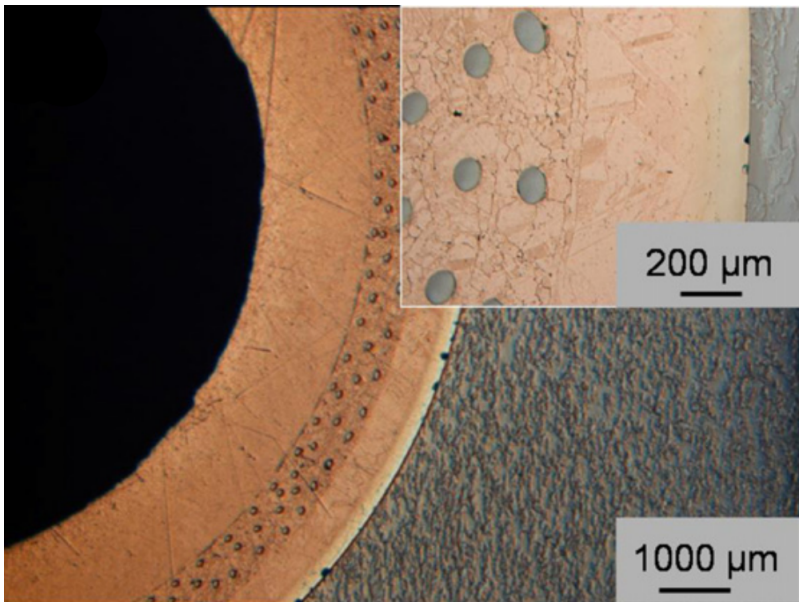

FIGURE 2.3: Cross-section of a W monoblock with a concentric W_f/Cu interlayer [27].

The simplest method to reduce stress at a bimaterial joint is to introduce an interlayer with properties between those of the joined materials. For monoblock designs, the interlayer is an annulus placed concentrically around the cooling tube. Figure 2.3 shows the W_f/Cu interlayer tested by Herrmann et al. in [27]. Planar interlayers are used at the heat-sink/armor interface of flat-tile designs. A planar interlayer made from a fiber-reinforced composite laminate (Figure 2.4) was studied by You in [28].

Interlayers need not consist of only one material. Functionally-graded interlayers, with a smooth or stepped progression of properties, form a more gradual transition between dissimilar materials. The melt-infiltrated porous tungsten composites presented in [21] were developed with this use in mind. Components fabricated with a three-zone interlayer faired well under cyclic HHF loads when tested by Greuner et al. [29].

Designers are not limited to the use of interlayers; stress-reducing mechanisms may extend into the body of the heatsink as well. Sun et al. analyzed a design combining a functionally-graded interlayer with tungsten wires embedded into the body of the heatsink [30].

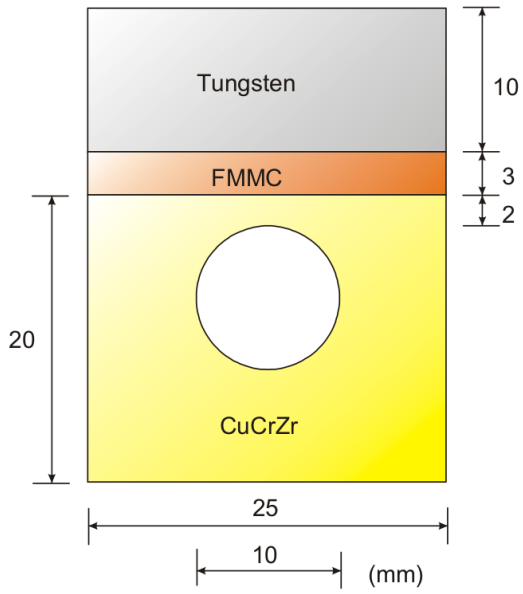

FIGURE 2.4: Schematic cross-section of a flat-tile divertor component with a composite interlayer [28].

2.3 Additive manufacturing with Selective Laser Melting

The design techniques discussed in the previous section are limited by their reliance on traditional processes for manufacturing tungsten components. Tungsten's intrinsic hardness and brittleness make it a difficult raw material to work with, which generally restricts tungsten components to very simple geometries. Additive manufacturing (AM) is an alternative to traditional processes; the design freedom afforded by AM could be key to producing better W-armored PFCs. This section provides an overview of AM and its implementation for metallic materials, and is based on the general references [31] and [32].

Irrespective of the mechanics of the build process, all AM processes follow the same general procedure. Starting from a 3D model, the surface of the component is triangulated and exported in a suitable format (e.g. the STL data format). The 3D model is typically produced in parametric CAD software, but other sources may be used. The triangulated surface data is then imported into pre-processing software that slices the model into layers and prepares a program for the machine. This software is typically machine-specific and provided by the machine's manufacturer. During the build process, the component is built up layerwise. After the machine builds the component from the processed 3D model, the component is removed from the machine and post-processed as necessary. The necessary post-build steps vary significantly between processes.

Compared to traditional manufacturing, process times for AM are long and the cost of raw materials is high. However, the extra expense of AM is offset by the advantages of sequential layerwise construction. AM has the ability to produce components with nearly arbitrary shape. Whereas the cost of a traditionally manufactured part is strongly influenced by its complexity, complexity has little impact on the cost of an AM part. This yields numerous benefits:

- Leadtimes for prototypes are reduced, shortening the design phase of product development.
- Parts can be built with complex geometries that would be otherwise impossible with traditional manufacturing processes.
- Subcomponents of an assembly can be merged, combining multiple functions into a monolithic part.
- Parts that would normally require custom tooling (e.g. injection molds, machining fixtures) can be produced directly instead. This makes small-batch production more economical.

A wide variety of AM processes exists for each class of materials: polymers, metals, and ceramics. *Selective Laser Melting* (SLM) is one of the most widely-employed processes for metals (alternative designations are *Laser Beam Melting* and *Direct Metal Laser Sintering*). SLM is a "powder-bed fusion" process; parts are built by selectively fusing regions of a thin layer of loose powder into a solid body. The powder is melted with a high-power laser – peak powers of 200 - 400W are typical. Between laser exposures, the platform onto which the manufactured components are built is lowered, and a new layer of powder is spread across the build container. Figure 2.5 shows a schematic representation of SLM.

SLM components generally require post-build heat treatment to relieve residual stress and machining to produce precision surfaces. *Hot isostatic pressing* (HIP) can also be used to reduce bulk porosity [34].

Parts made with SLM already see commercial application. For example, new generations of Airbus aircraft fly with engines containing AM fuel nozzles [35]. SLM has been demonstrated with many metals, from lightweight structural metals like aluminium and titanium to biocompatible alloys for orthopedic implants.

2.3.1 Selective Laser Melting of tungsten

While more commonly used metals already see commercial application in AM form, SLM of pure tungsten is still in its infancy. There are only a handful of

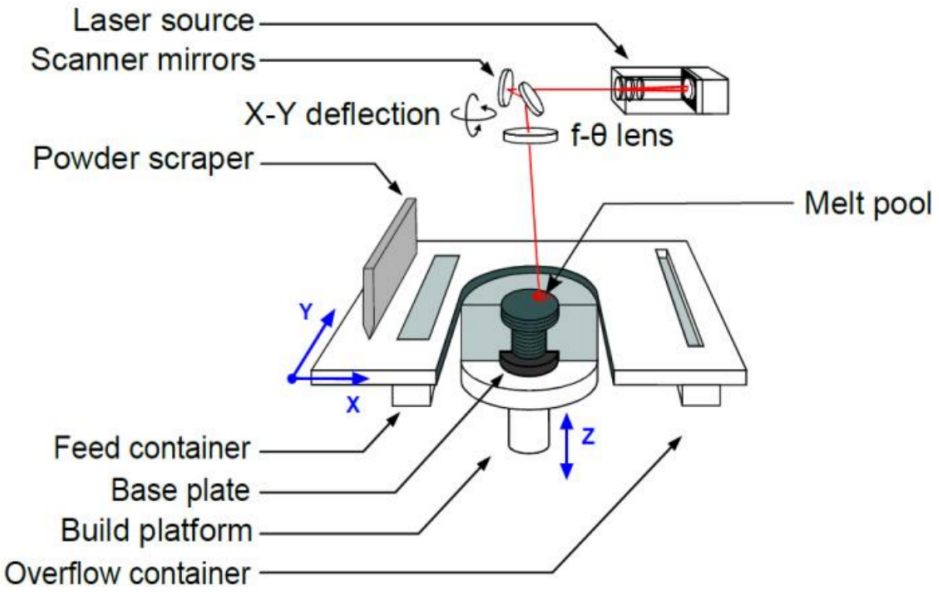

FIGURE 2.5: Schematic of the SLM build process [33].

works on this topic to date. The results indicate that the physical properties of tungsten make it a challenging material to process with SLM.

One of the main focuses of contemporary research on the subject is fabricating samples with a high relative mass density. Zhou et al. remark that the combination of the high melting temperature, high thermal conductivity, high melt viscosity, and oxidation tendency of tungsten makes it difficult to maintain a continuous molten track during laser melting. The melt pool tends to ball into droplets with poor wetting properties that solidify into material with a high degree of porosity. Using commercially-available polyhedral tungsten powder, samples with a maximum of only 82.9% of theoretical density were achieved [36]. Wang et al. determined that plasma spheroidization of polyhedral tungsten powder increases powder packing density and laser absorptivity. These improvements yielded samples with densities up to 96% of the theoretical maximum [37].

Von Müller et al. achieved SLM tungsten samples with minimal porosity - up to 98% of theoretical density. However, micrographs of the samples reveal another challenge: SLM tungsten exhibits widespread cracking at grain boundaries (see Figure 2.6). The cracking is attributed to residual stresses that result from extreme local thermal gradients during laser melting. Additionally, the thermomechanical properties of tungsten make it more susceptible to thermal stress than most other metals [38]. The influence of material properties on crack-inducing residual stresses in metals processed by SLM was investigated by Vrancken et al. in [39], and a complete discussion by Vrancken on the

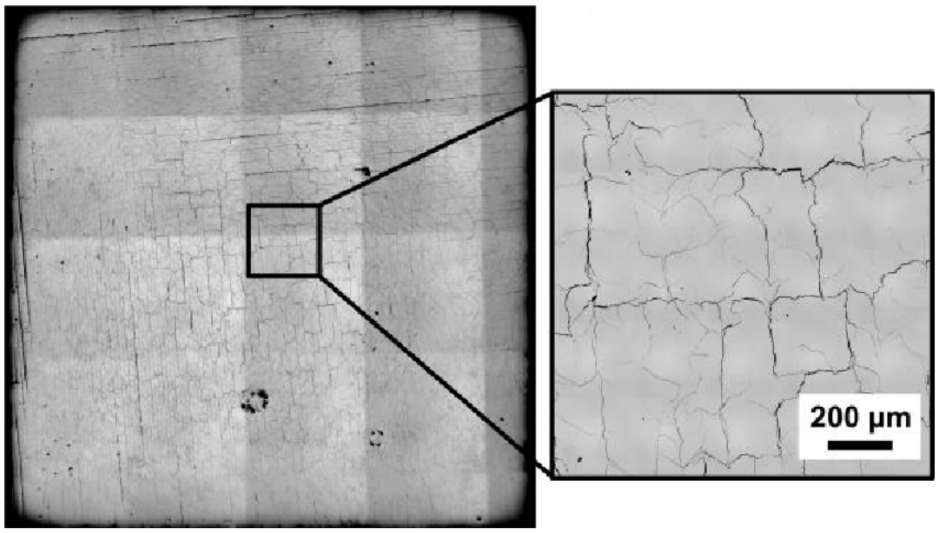

FIGURE 2.6: Optical micrograph perpendicular to the build direction of SLM tungsten samples produced with a laser power of 400 W and a laser scanning speed of 300 mm/s [38].

nature of residual stress in metals produced by SLM is available in [40]. The authors found no clear correlation between measurable thermal stresses and individual material properties or combinations thereof. They remark that residual stresses are the product of too many interconnected phenomena to be predicted adequately. However, one means to semi-quantitatively characterize the stress that develops during thermal transients is to use the following metric from [41]:

$$\sigma \propto \frac{\alpha_m E \Delta T}{1 - \nu} \tag{2.1}$$

where ΔT is the difference between the material's melting temperature and the base plate preheat temperature. Application of this metric by von Müller et al. shows that the value for tungsten ranges between 1.57 and 5.35 times that of other metals commonly produced with SLM, which indicates tungsten has a strong tendency to develop thermal stress due to temperature transients. The authors suggest preheating the base plate above the DBTT of tungsten to mitigate cracking [38]. Kurzynowski et al. suggested alloying tungsten with elements such as Co, Re, or Ti to improve ductility or using HIP to reduce porosity after fabrication [42].

There remains much to be done on the topic of AM with tungsten. Recent research has focused mainly on the first step of SLM process development with a new material: achieving samples with high relative density and acceptable microstructure. As yet, no published works have experimentally characterized the material's mechanical and thermal properties. Data from this step will be

vital for detailed analyses of W_{AM}/Cu composite components.

2.4 Additively manufactured composite structures

Because of the exceptional design freedom of AM, AM microstructures may take many forms. For W_{AM}/Cu structures made using SLM, the most important design constraint is that the AM tungsten structure must be open to facilitate the removal of residual powder and subsequent melt infiltration. Numerous options exist that meet this requirement. Two common structures, which will be used to demonstrate the design methodology presented in this work, are discussed here: lattices and regular honeycomb.

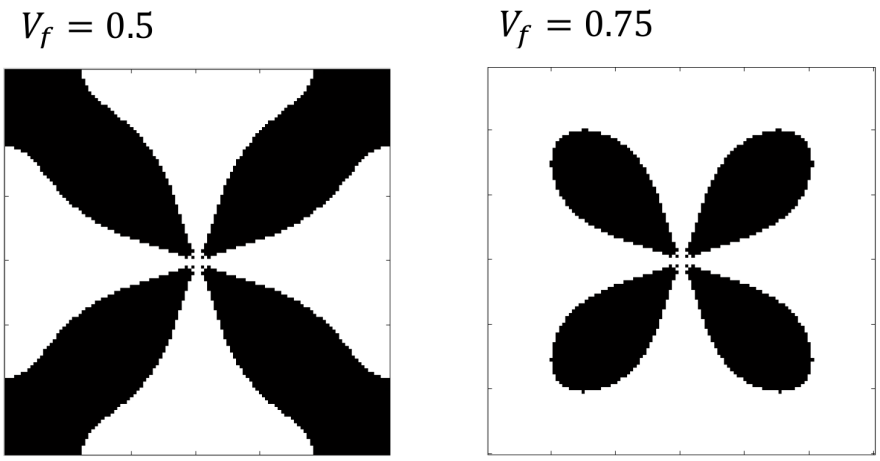

FIGURE 2.7: Unit cell of a 2D W/Cu microstructure optimized for minimal thermal expansion [43].

AM has made the use of lattice structures practical for an increasing number of applications. Topology-optimized components, for example, can be designed in multiple ways using lattices of variable volume fraction [44]. Fabrication of these structures is generally only possible with AM. The extremely large variety of potential lattice geometries complicates the selection of a promising candidate for stress-reduction in PFCs. Topology optimization of 2D W/Cu microstructures for minimal thermal expansion was performed by von Müller et al. [43]. The resulting topology, shown in Figure 2.7, suggests that a truss-like cubic lattice would be the most likely extension to three dimensions.

An advantage of truss-like lattice structures is the relative ease with which they can be used to design components. McMillan et al. explain the procedu-

ral generation of truss-like lattices in STL format for use with AM [45].

Because of their simple, 2D geometry, honeycomb materials are easy to produce and have a long history of use. Thin-walled honeycomb commonly serves as the core material of laminated sandwich-structured composites due to its low density, high out-of-plane shear stiffness, and in-plane elastic isotropy. Designing functionally graded or topology-optimized structures with honeycomb materials is also straight-forward. For example, the local volume fraction can be set easily by adjusting the wall thickness of a honeycomb with a uniform cell size.

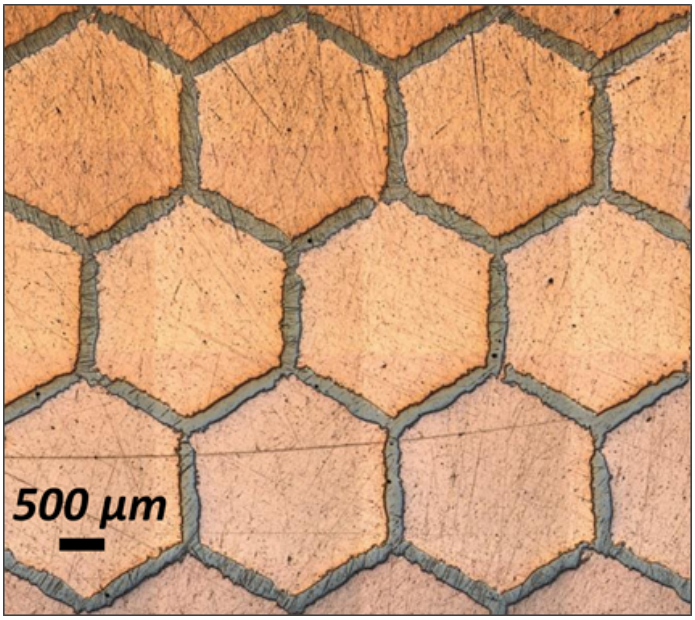

FIGURE 2.8: Copper-infiltrated AM-tungsten honeycomb created by the Plasma Component Interaction research group at the Max Planck Institut for Plasma Physics in Garching.

Traditionally, AM lattices and honeycomb are open structures; the space between struts and cell walls remains empty. In this case, analytical beam and truss models can be employed to estimate the structure's material properties (e.g. [46]). However, melt-infiltration of a tungsten structure with copper alloys produces a solid body (e.g. the W_{AM}/Cu honeycomb in Figure 2.8). Estimation of the composite's material properties can no longer be performed analytically. Properties must be calculated by homogenization.

2.4.1 Theory of homogenization

A defining feature of composite materials is their heterogeneous microstructure, which exists even in components with a macroscopically homogeneous material distribution. A full description of a composite component's physical behavior requires analysis at both length scales. However, simulating macroscopic structures with a mesh fine enough to capture the full detail of the composite microstructure would produce a numerical system too large to solve by practical means. To efficiently simulate structures built from composite materials, analysis must be performed at the macro- and microscopic scales separately.

This dual-scale description of material behavior is accomplished by averaging the heterogeneous properties of the composite microstructure over a representative volume element (RVE), a process known as homogenization. The homogenized material properties form the link between simulations at the macro- and microscale. The fundamental theory of this technique, as described in the following, is outlined by Hassani and Hinton in [47].

Homogenization is based on a material description wherein the microstructure is considered periodic and its characteristic size is much smaller than the size of the macroscopic structure. A 3D medium is periodic if its properties can be described by functions with the following character:

$$g\left(\boldsymbol{x} + \mathcal{N}_y \boldsymbol{Y}\right) = g\left(\boldsymbol{x}\right) \tag{2.2}$$

where $\boldsymbol{x}$ is the position of any point in the body, $\boldsymbol{Y}$ is a constant vector representing the dimension and orientation of the microstructure's periodic unit cell, and $\mathcal{N}_y$ is a matrix with arbitrary integers n_1, n_2, and n_3 of the form

$$\mathcal{N}_y = \begin{bmatrix} n_1 & 0 & 0 \\ 0 & n_2 & 0 \\ 0 & 0 & n_3 \end{bmatrix} \tag{2.3}$$

Any tensorial quantity (e.g. density, constitutive relations) may be represented in this way. Although these quantities generally experience rapid local variation at the microscopic level, variation at the macroscale is seen to be smooth. This motivates an asymptotic expansion of the modelled physical quantities, whereby coordinates in the unit-cell coordinate system $\mathbf{Y}$ are related to those in the global coordinate system $\mathbf{X}$ by

$$\epsilon\, y_i = x_i \tag{2.4}$$

The small parameter ϵ describes the ratio of micro- to macroscale dimensions. The value $1/\epsilon$ can be understood as a "magnification factor" that enlarges the composite microstructure to the macroscopic structural dimensions. Functions

in the composite body are then defined in terms of both $\boldsymbol{x}$ and $\boldsymbol{y}$. In the context of this dual-scale description, functions defining material behavior (e.g. displacement, stress) can be expanded generally as

$$\phi(\boldsymbol{x}) = \phi_0(\boldsymbol{x}, \boldsymbol{y}) + \epsilon\phi_1(\boldsymbol{x}, \boldsymbol{y}) + \epsilon^2\phi_2(\boldsymbol{x}, \boldsymbol{y}) + \dots \tag{2.5}$$

where ϵ is assumed to approach 0 and each function $\phi_n(\boldsymbol{x}, \boldsymbol{y})$ is $\mathbf{Y}$-periodic and smooth with respect to $\boldsymbol{x}$.

Hassani and Hinton demonstrate the basic principle of homogenization using one-dimensional elasticity as an example. They show that the homogenized Young's modulus E_1^H of a one-dimensional composite is found with

$$\frac{1}{E_1^H} = \frac{1}{|Y|}\int_0^Y \frac{1}{E_1(y)}dy \tag{2.6}$$

This amounts to a volumetric averaging of compliance on the unit cell $\mathbf{Y}$. Based on their treatment of general elliptic boundary-value problems in non-homogeneous media, the authors arrive at the following for the homogenized elasticity tensor:

$$E_{ijkl}^H = \frac{1}{|Y|}\int_{\boldsymbol{Y}} \left(E_{ijkl} - E_{ijpq}\frac{\partial u_p^{kl}}{\partial y_q} \right) dY \tag{2.7}$$

where the Einstein summation convention applies. The displacements $\boldsymbol{u}^{kl}$ are solutions to

$$\int_{\boldsymbol{Y}} \frac{\partial(\delta u_i)}{\partial y_j} \left(E_{ijpq}\,\varepsilon_{pq}^{0(kl)} - E_{ijpq}\frac{\partial u_p^{kl}}{\partial y_q} \right) dY = 0 \tag{2.8}$$

with periodic boundary conditions. One displacement field $\boldsymbol{u}^{kl}$ is necessary for each unique strain component (three components in 2D, six in 3D). Given a set of displacement vectors, (2.7) can be used to explicitly calculate the homogenized elastic properties. Conceptually, the solution of (2.8) can be understood as determining the displacements that result from applying a unit strain $\varepsilon_{pq}^{0(kl)}$ to the periodic unit cell. While (2.8) is used by the majority authors, (2.9) is common as an alternative to (2.7). It is used by Sigmund and Torquato in [48] and Andreassen and Andreasen in [49], for example.

$$E_{ijkl}^H = \frac{1}{|Y|}\int_{\boldsymbol{Y}} \left(\varepsilon_{pq}^{0(ij)} - \varepsilon_{pq}(\boldsymbol{u}^{ij})\right)\, E_{pqrs}\, \left(\varepsilon_{rs}^{0(kl)} - \varepsilon_{rs}(\boldsymbol{u}^{kl})\right) dY \tag{2.9}$$

This performs a volumetric averaging of the difference between the applied unit strains and the actual local strains that occur due to the displacements $\boldsymbol{u}$. In summary, using the homogenized elastic properties of a composite involves three steps:

1. Solve (2.8) with $\boldsymbol{Y}$-periodic boundary conditions for each $\boldsymbol{u}^{kl}$.

2. Evaluate the homogenized coefficients with (2.7) or (2.9).

3. Apply the homogenized coefficients in the macroscale analysis.

Despite the simplicity of (2.7), (2.9) is preferred in this work because it can be easily modified to calculate a composite's homogenized coefficient of thermal expansion (CTE). A composite's thermoelastic tensor, defined as

$$\beta_{ij} = E_{ijkl}\,\alpha_{kl} \tag{2.10}$$

combines the elasticity tensor and thermal expansion tensor. It can be homogenized using

$$\beta_{ij}^{H} = \frac{1}{|Y|}\int_{\boldsymbol{Y}} \left(\alpha_{pq} - \varepsilon_{pq}(\boldsymbol{u}^{\alpha})\right)\, E_{pqrs}\, \left(\varepsilon_{rs}^{0(ij)} - \varepsilon_{rs}(\boldsymbol{u}^{ij})\right) dY \tag{2.11}$$

where the displacement $\boldsymbol{u}^{\alpha}$ results from solving (2.8) using the thermal expansion tensor as an applied unit strain:

$$\int_{\boldsymbol{Y}} \frac{\partial(\delta u_i)}{\partial y_j}\left(E_{ijkl}\alpha_{kl} - E_{ijpq}\frac{\partial u_p^{\alpha}}{\partial y_q}\right) dY = 0 \tag{2.12}$$

The homogenized thermal expansion tensor is then calculated with

$$\alpha_{ij}^{H} = (E_{ijkl}^{H})^{-1}\,\beta_{kl}^{H} \tag{2.13}$$

Because of the similarities between elasticity and thermal conduction, the homogenized thermal conductivity can be found in a similar manner. The analog to the displacements $\boldsymbol{u}^{kl}$ are the temperature fields T^{j}, which are found by applying unit temperature gradients to $\boldsymbol{Y}$ with periodic boundary conditions:

$$\int_{\boldsymbol{Y}} \frac{\partial(\delta T)}{\partial y_i}\left(\kappa_{ip}\frac{\partial T}{\partial y_p}^{0(j)} - \kappa_{ip}\frac{\partial T^{j}}{\partial y_p}\right) dY = 0 \tag{2.14}$$

The homogenized thermal conductivity tensor is then found with

$$\kappa_{ij}^{H} = \frac{1}{|Y|}\int_{\boldsymbol{Y}} \left(\frac{\partial T}{\partial y_m}^{0(i)} - \frac{\partial T^{i}}{\partial y_m}\right)\kappa_{mn}\left(\frac{\partial T}{\partial y_n}^{0(j)} - \frac{\partial T^{j}}{\partial y_n}\right) dY \tag{2.15}$$

For simple unit cells, such as rank-1 and rank-2 laminates, homogenization can be performed analytically, as shown in [50]. However, complex domains require the use of numerical techniques. The finite-element implementation of these homogenization techniques is detailed in Section 3.1.

2.5 Structural topology optimization

The design approaches for PFCs discussed in Section 2.2.2 all share a fundamental limitation: they rely on geometrically simple stress-reducing mechanisms. Functionally-graded transition regions, for example, are likely only possible with planar interlayers. The ability to produce complex composite structures with AM frees designers of the majority of manufacturing constraints, facilitating a vast range of new possible designs. The possibilities are so varied, in fact, that profitable exploitation of AM requires an equally capable design approach. Topology optimization can be employed to determine the optimal material distribution in a PFC exposed to HHF loads with the goal of reducing thermal stresses. This powerful technique complements AM well, and has its roots in the field of structural design.

A thorough overview of the field of structural optimization is provided in [51]. Structural optimizations almost always result in nonlinear mathematical problems. The system equations used to evaluate the objective and constraints are, in most cases, not only highly nonlinear, but are also implicit functions of the design variables. As such, evaluation of these equations and their sensitivities is frequently the most computationally intensive step of any optimization. Additionally, most structural optimization problems are non-convex; special care must be taken to ensure that an "optimal" solution produced by the algorithm is in fact a global optimum. Another general aspect to consider when applying the solutions of optimization problems to design is that optimization only considers objectives and constraints that can be formulated mathematically. Optimization is thus a tool to be used in concert with the experience and intuition of the designer.

The concept of topology optimization for continua was first introduced by Bendsøe and Kikuchi in 1988. The authors formulated a design problem whereby the optimal distribution of material in a given design domain is determined with the goal of minimizing the structure's compliance under an applied load (ie. maximizing stiffness) [52]. Unlike traditional techniques in structural optimization, such as size and shape optimization, which require preliminary assumptions about the optimal structure's form, topology optimization does not restrict designs to a prescribed configuration. Figure 2.9 shows an example of a 2D structure optimized for minimum compliance. Topology optimization is often used in conjunction with size and shape optimization, where the latter are used to fine-tune the optimized topology. The design study performed by Crescenzi et al. in [53] demonstrates the use of size optimization for PFCs.

Interest in topology optimization has grown considerably since the publication of [52]. Sigmund and Maute performed a thorough review of intervening developments in [55]. Of the many approaches to numerical topology optimization, the density-field approach is the most relevant for this work. The structure's

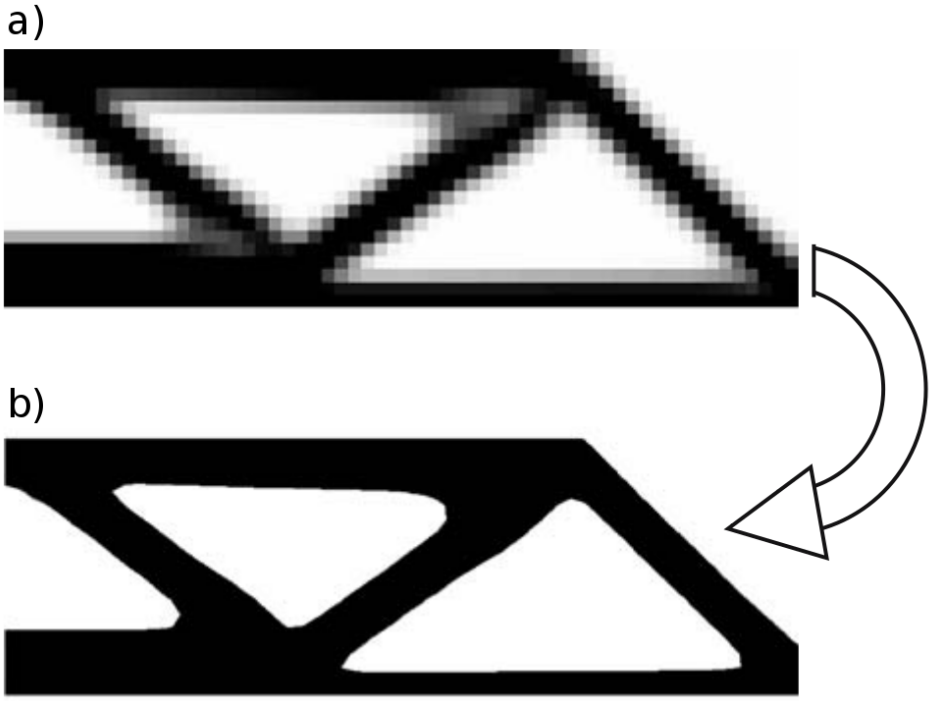

FIGURE 2.9: Topology optimization for minimum compliance with a load applied at the bottom-right corner: a) raw output, and b) after post-processing [54].

shape is represented by a density field, which is typically discretized with one design variable per element. For traditional stiffness- and stress-based structural optimization, the design variables are continuous and represent a relative material density. They range between 0 and 1, where 0 represents void and 1 solid material. Topology optimization techniques can be further categorized by the optimization algorithm used to seek optimal solutions; optimality criteria methods and mathematical programming are common alternatives.

Density-field approaches to topology optimization are typically prone to mesh-related problems. Mesh refinement tends to produce entirely new topologies, since a finer discretization allows the algorithm to represent ever finer details. Bilinear finite elements, especially, often produce undesirable "checkerboard" patterns [54]. Many techniques exist to mitigate these issues. The simplest, heuristic approaches apply a filter to the mesh, averaging an element's design variable or its sensitivity with those of surrounding elements. Other techniques expand the optimization problem with constraints imposed on the structure's perimeter, density field gradient, etc. Filter-based techniques are derived from the field of image processing, and were introduced by Sigmund in [56]. A sensitivity filter such as (2.16) is used by many authors, where $w(\boldsymbol{x}_e)$ is a function that weights neighboring elements based on their centroid $\boldsymbol{x}_e$.

$$\frac{\partial f}{\partial \rho_j}^* = \frac{\sum_e w(\boldsymbol{x}_e)\,\rho_e\,\frac{\partial f}{\partial \rho_e}}{\sum_e w(\boldsymbol{x}_e)\,\rho_e} \tag{2.16}$$

Although early work on topology optimization avoided stress-based objectives and constraints due to their computational complexity, treatment of stress is highly desirable. Indeed, the premise of this work is the minimization of stress. A more traditional example is the augmentation of the minimum compliance problem with stress constraints to prevent yielding.

There are a variety of approaches to treating stress in topology optimization. As an inherently local quantity with a (generally) known limit, stress is most naturally constrained locally (e.g. with one constraint per element). This approach requires a large number of highly nonlinear constraints, however, which increases the size of the optimization problem, and adds considerably to the computational complexity. An alternative is to aggregate local stresses into a global stress metric, an approach proposed by Yang and Chen in [57]. One example of a suitable global stress metric is the p-norm of local stress values (2.17). Using a global metric reduces the computational effort required to treat stress in optimization problems, but is not without disadvantages. Yang and Chen note that the global stress metrics they tested were sensitive to parameters of the solution-search algorithm, and exhibited numerical instability in some cases. Additionally, this method places a constraint only on a global "summary" of the stress state in the body; Duysinx and Sigmund found that local stress values are only weakly constrained and may therefore exceed the desired limit in some locations. They also demonstrated a third approach to treat stress: minimization of the maximum local stress over all elements. They comment that this was the most computationally expensive of the three approaches tested [58].

$$G_{kk} = \left[\int_\Omega \left(\frac{f_i(\sigma)}{f_{max}(\sigma)}\right)^p d\Omega\right]^{\frac{1}{p}} \tag{2.17}$$

Without special treatment, topology optimization problems that incorporate stress in objective or constraint functions generally experience numerical singularities. For problems where the material distribution ranges between solid material and void, singularities occur in elements of the design domain with material densities near zero due to a discontinuity of stress at zero density. A method known as "ϵ-relaxation" was developed in [59] to treat the degeneracy of stress relationships for discrete structures, and extended to continua in [60] and [58].

2.5.1 Method of Moving Asymptotes

Optimization problems in this work are solved using a mathematical programming technique known as the Method of Moving Asymptotes (MMA). It was introduced by Svanberg in [61], and expanded into a globally convergent algorithm in [62]. A general description of the MMA algorithm is presented below; further details concerning the implementation are found in [63].

In order to simplify the implementation of a wide variety of optimization problems, the MMA solves a standardized problem of the form

$$\begin{aligned} \min \quad & f_0(\boldsymbol{x}) + a_0 z + \sum_{i=1}^{m} \left[c_i y_i + \frac{1}{2} d_i y_i^2 \right] \\ \text{subject to} \quad & f_i(\boldsymbol{x}) - a_i z - y_i \leq 0, \qquad i = 1, \ldots, m \\ & \boldsymbol{x^{min}} \leq \boldsymbol{x} \leq \boldsymbol{x^{max}} \\ & \boldsymbol{y} \geq \boldsymbol{0} \\ & z \geq 0 \end{aligned} \tag{2.18}$$

The function f_0 is the optimization objective function, and each function f_i represents a constraint. The vector $\boldsymbol{x}$ contains n design variables x_j, which are each restricted to a range of realistic values between x_j^{min} and x_j^{max}. For topology optimization problems, these variables generally represent either a local material density (ranging from void to solid material) or, as is the case in this work, a parameter defining the makeup of a composite material.

The MMA extends the set of design variables to produce a more robust, versatile formulation. The artificial variables y_i and z are used to 1) traverse infeasible design points, and 2) tune the standardized problem to the desired formulation in conjunction with the constant parameters a_0, a_i, c_i, and d_i.

For each iteration k in the solution of problem (2.18), a subproblem is generated by approximating the functions $f_0, f_1, \ldots, f_m$ at the current solution point with convex, separable functions in the form of (2.19). Generating the subproblem requires evaluation of the system equations and their gradients (e.g. with a finite-element solver).

$$f_i(\boldsymbol{x}) \approx g_i^{(k)}(\boldsymbol{x}) = r_i^{(k)} + \sum_{j=1}^{n} \left[\frac{P_{ij}^{(k)}}{U_j^{(k)} - x_j} + \frac{Q_{ij}^{(k)}}{x_j - L_j^{(k)}} \right] \tag{2.19}$$

The parameters $U_j^{(k)}$ and $L_j^{(k)}$ are the "moving asymptotes" that define the domain of the approximate function. After the first two iterations of the problem, the moving asymptotes are either relaxed or tightened depending on the convergence behavior in previous iterations. A monotonic increase or decrease of a variable indicates stable convergence; the asymptotes can be relaxed to

accelerate convergence to the optimal solution. Oscillation of a design variable indicates instability; the asymptotes are tightened to shrink the region in which the approximation is considered a valid representation of the original function. The coefficients $P_{ij}^{(k)}$, $Q_{ij}^{(k)}$, and $r_i^{(k)}$ are derived from the values and gradients of the system equations evaluated at the current solution point.

The optimal solution of the subproblem is found using a primal-dual solution method. The inequality constraints f_i are converted to equality constraints with the additional slack variables s_i. Each design variable is restricted to a region between two move limits, α_j and β_j, that are determined in consideration of their natural limits x_j^{min} and x_j^{max} and the moving asymptotes $L_j^{(k)}$ and $U_j^{(k)}$. The corresponding Lagrange function is

$$\mathcal{L} = g_0(\boldsymbol{x}) + (a_0 - \zeta)z + \sum_{j=1}^{n} [\xi_j(\alpha_j - x_j) + \eta_j(x_j - \beta_j)] + \sum_{i=1}^{m} \left[\lambda_i(g_i(\boldsymbol{x}) - a_i z - y_i + s_i) + c_i y_i + \frac{1}{2} d_i y_i^2 - \mu_i y_i\right] \quad (2.20)$$

where all Lagrange multipliers (λ_i, ξ_j, η_j, μ_i, and ζ) are nonnegative. Slackness of the Lagrange multipliers is ensured by using relaxed conditions (e.g. $\zeta z - \epsilon = 0$), where the positive parameter ϵ is progressively reduced to a very small value. The optimum of the primal-dual subproblem is found iteratively via line-search using a Newton search direction. After the subproblem has been solved, the system equations and their gradients are reevaluated at the new solution point, and a new approximate subproblem is formed for the next iteration.

The MMA has a number of features that make it particularly suitable for structural optimizations. As discussed in Section 2.5, structural optimizations are highly nonlinear, non-convex, and require time-consuming evaluation of implicit system equations. These issues are mitigated by the novel form of the MMA's approximating functions (2.19): though still nonlinear, they are convex, separable, and explicit. Convexity guarantees the subproblem has a unique optimum. For systems with a large number of design variables, separability and explicit evaluation greatly reduce the expense of determining the search direction and evaluating potential solution points during the line-search. Due to these advantages, the MMA sees extensive use in the field of topology optimization.

Chapter 3

Additively manufactured W/Cu composites

Topology optimization of components with AM composite structures requires as an input a model to evaluate the physical properties of the composite and their sensitivities at all material compositions. This material model depends on the microstructural topology of the composite. In Section 4.4, the topology-optimization code is demonstrated with two common microstructures: regular honeycomb and a body-centered cubic (BCC) lattice. The thermomechanical properties of open lattice structures and thin-walled honeycomb are relatively well known. As mentioned in Section 2.4, their properties can be estimated with decent accuracy using analytical models. However, these models are of little use when the open structures are melt-infiltrated. Properties of the solid bodies produced in this way must be determined numerically or experimentally.

Because W_{AM}/Cu composites are such a new development, experimental characterization has yet to be performed. For materials without a database of experimental results, a simple approximation, such as linear rule-of-mixtures interpolation, yields usable results, but more realistic modelling of the composite's properties should ultimately produce better designs. For that reason, material models for the investigated composites were produced by numerical homogenization.

3.1 Numerical homogenization

Although the topology optimization code *TopOpt*, detailed later, was only applied to 2D domains, homogenization of material properties was done in three dimensions for the structures considered. Most AM microstructures – lattices in particular – are inherently 3D, and cannot be simplified to two dimensions. Some, such as honeycomb, may be simplified to 2D to estimate their in-plane properties. However, as is the case for PFCs, the structure may be used in an

orientation that requires knowledge of the out-of-plane properties as well. In this case, homogenization must be performed in three dimensions.

Because of the large temperature gradients in a PFC at high heat fluxes, the temperature dependence of material properties should be modelled. The homogenization code should therefore produce a two-variable material model, parameterized by material composition and temperature.

Existing homogenization codes did not provide a convenient means to satisfy both of these requirements. Therefore, the code to perform these calculations was developed as part of this work, and is referred to as *homog3d*. The following describes the calculation of homogenized material properties in 3D as implemented in *homog3d*. Section 3.2 presents the results of the homogenization process for CuCrZr-infiltrated tungsten honeycomb and BCC lattices.

Homogenization theory was discussed in Section 2.4.1. Due to the geometric complexity of the considered composites, analytical solution of the equations of homogenization on a representative 3D volume element is not practical. The process is therefore performed with a finite-element numerical approximation. The formulas of Section 2.4.1 are transformed here to use the more convenient matrix/vector notation. The FE formulation is set forth in Appendix A, which can be referenced for a more detailed description of the notation used.

First, tensorial quantities are translated to their respective matrix/vector form. The rank-4 elasticity tensor E_{ijkl} is transformed to the matrix with coefficients $\mathcal{C}_{rs}$. As a rank-2 tensor, thermal conductivity can be represented directly by the matrix with coefficients κ_{ij}. The thermal expansion (α_{ij}) and thermoelastic (β_{ij}) tensors can be represented as vectors using the same format as for strain and stress.

Second, continuous field variables must be discretized. The displacements $\boldsymbol{u}^{kl}$ are discretized within an element e the same as any general displacement vector:

$$\boldsymbol{u}^{kl(e)} = \begin{bmatrix} \boldsymbol{N}^{(e)T} & 0 & 0 \\ 0 & \boldsymbol{N}^{(e)T} & 0 \\ 0 & 0 & \boldsymbol{N}^{(e)T} \end{bmatrix} \boldsymbol{d}_s^{(e)} \tag{3.1}$$

where $\boldsymbol{d}_s^{(e)}$ are the 3D discrete displacements corresponding to the s-th applied unit strain, with a form that matches (A.15). After these transformations, (2.8) becomes

$$\sum_{e=1}^{n_{el}} \int_{\boldsymbol{Y}^{(e)}} (\mathcal{B}^{(e)}\, \delta\boldsymbol{d}^{(e)})^T \left(\mathcal{C}^{(e)} \boldsymbol{\varepsilon}_s^0 - \mathcal{C}^{(e)}\, \mathcal{B}^{(e)}\, \boldsymbol{d}_s^{(e)}\right) dY = 0 \tag{3.2}$$

In 3D, the s-th applied unit strain $\boldsymbol{\varepsilon}_s^0$ is a 6-vector, and contains only one non-zero component. The unit normal strain along the X-axis, for example, would take the form

$$\boldsymbol{\varepsilon}_1^0 = \begin{bmatrix} 1 & 0 & 0 & 0 & 0 & 0 \end{bmatrix}^T \tag{3.3}$$

Multiplication with the elasticity matrix yields the s-th column: $\boldsymbol{c}_s^{(e)}$. The similarities to a traditional FE system are evident in (3.2). Element stiffness matrices are built by integrating the local elasticity matrix $\mathcal{C}^{(e)}$ and strain-displacement matrices $\mathcal{B}^{(e)}$ as for any FE problem (A.18). Unit strains are applied to the mesh as load vectors, computed with (3.4). The system is solved once for each unit strain.

$$\boldsymbol{f}_s^{(e)} = \int_{\boldsymbol{Y}^{(e)}} \mathcal{B}^{(e)^T} \boldsymbol{c}_s^{(e)} \, dY \tag{3.4}$$

Solving (3.2) must be done with periodic boundary conditions to ensure that the displacement fields $\boldsymbol{d}_s$ are $\boldsymbol{Y}$-periodic. If the composite's unit cell is cuboid and can be discretized with a structured mesh, ensuring each boundary node matches directly with a node on the opposing boundary, these conditions can be applied by equating the displacements of the matching nodes. When using an unstructured mesh, where a boundary node generally does not have a matching node on the opposing boundary, periodic boundary conditions must be applied with a combination of Dirichlet constraints and multi-point constraints (e.g. with Lagrange multipliers or the penalty method).

The mesh becomes constrained as depicted in Figure 3.1 for a 2D composite with a rectangular unit cell. When applying unit normal strains, displacements normal to the boundary on all boundary faces are fixed. For unit shear strains, the boundary conditions depend on which strain component is applied. Consider the 4th strain component as an example (shear in YZ-plane). This shear represents a rotational deformation about the X-axis. The periodic boundary conditions for this unit strain fix boundary displacements normal to the X-boundaries. On the Y- and Z-boundaries, displacements *within the boundary plane* are fixed; *normal* boundary displacements remain free.

By then discretizing (2.9), the homogenized coefficients of the elasticity matrix can be evaluated by summing contributions from each element:

$$\mathcal{C}_{rs}^H = \frac{1}{|Y|} \sum_{e=1}^{n_{el}} \int_{\boldsymbol{Y}^{(e)}} \left(\boldsymbol{\varepsilon}_r^0 - \mathcal{B}^{(e)} \, \boldsymbol{d}_r^{(e)}\right)^T \mathcal{C}^{(e)} \left(\boldsymbol{\varepsilon}_s^0 - \mathcal{B}^{(e)} \, \boldsymbol{d}_s^{(e)}\right) dY \tag{3.5}$$

The corresponding elastic constants (E_x, ν_{xy}, etc.) can be found by inverting the resultant elasticity matrix to produce the compliance matrix $\mathcal{S}^H$. Thermal expansion is homogenized by first applying the thermal expansion tensor as a strain load:

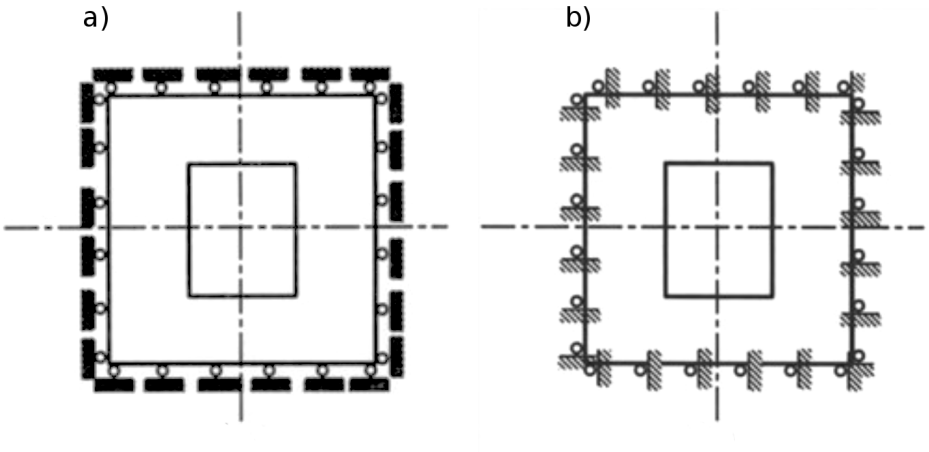

FIGURE 3.1: Periodic boundary conditions for homogenization of a 2D composite with rectangular microscale voids [50]. For unit normal strains, a) is used. For unit shear strains, b) is used.

$$\boldsymbol{f}_{\alpha}^{(e)} = \int_{\boldsymbol{Y}^{(e)}} \mathcal{B}^{(e)^T} \mathcal{C}^{(e)} \, \boldsymbol{\alpha}^{(e)} dY \tag{3.6}$$

The homogenized *thermoelastic* tensor is then found with

$$\beta_r^H = \frac{1}{|Y|} \sum_{e=1}^{n_{el}} \int_{\boldsymbol{Y}^{(e)}} \left(\boldsymbol{\alpha}^{(e)} - \mathcal{B}^{(e)} \, \boldsymbol{d}_{\alpha}^{(e)} \right)^T \, \mathcal{C}^{(e)} \, \left(\boldsymbol{\varepsilon}_r^0 - \mathcal{B}^{(e)} \, \boldsymbol{d}_r^{(e)} \right) dY \tag{3.7}$$

For components 1 - 3 of the thermoelastic tensor (normal strains), the displacements $\boldsymbol{d}_{\alpha}$ are solved using periodic boundary conditions matching Figure 3.1a. For the remaining components, which correspond to shear strains, boundary conditions are applied as in Figure 3.1b. Multiplication with the homogenized compliance matrix then yields the thermal expansion tensor:

$$\boldsymbol{\alpha}^H = \mathcal{S}^H \boldsymbol{\beta}^H = (\mathcal{C}^H)^{-1} \boldsymbol{\beta}^H \tag{3.8}$$

Discretization of the thermal conductivity problem proceeds similarly. As for elasticity, the global system matrix is built in the standard method (A.5). The load vector is used to apply a unit temperature gradient $\boldsymbol{\phi}_j^0$ to the volume along the j-th coordinate axis:

$$(\boldsymbol{f}_{\boldsymbol{q}}^{(e)})_j = \int_{\boldsymbol{Y}^{(e)}} \mathcal{F}^{(e)^T} \kappa^{(e)} \boldsymbol{\phi}_j^0 dY = \int_{\boldsymbol{Y}^{(e)}} \mathcal{F}^{(e)^T} \boldsymbol{k}_j^{(e)} dY \tag{3.9}$$

This can be simplified to the j-th column of the conductivity tensor: $\boldsymbol{k}_j^{(e)}$. Periodic boundary conditions are applied with the same techniques used for

homogenizing elasticity and thermal expansion. This is simplified somewhat for the thermal conductivity problem, since the field variable is a scalar. With the resulting discrete temperature fields $\boldsymbol{\theta}_j$, the coefficients of the homogenized thermal conductivity tensor are determined via the discrete form of (2.15):

$$\kappa_{ij}^H = \frac{1}{|Y|} \sum_{e=1}^{n_{el}} \int_{\boldsymbol{Y}^{(e)}} \left(\boldsymbol{\phi}_i^0 - \mathcal{F}^{(e)} \boldsymbol{\theta}_i^{(e)} \right)^T \kappa^{(e)} \left(\boldsymbol{\phi}_j^0 - \mathcal{F}^{(e)} \boldsymbol{\theta}_j^{(e)} \right) dY \tag{3.10}$$

A composite's RVE can be discretized in a number of ways. The Matlab script presented in [49] demonstrates discretization of 2D domains with a uniform structured mesh of quadrilateral elements. The material distribution can be visualized as a raster image with individual materials displayed as a unique color, where each pixel represents one element.

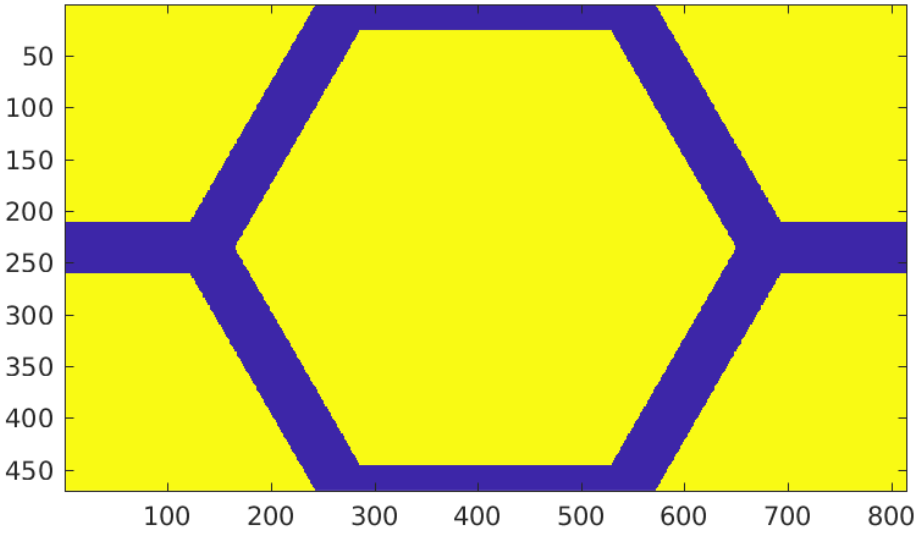

FIGURE 3.2: Material distribution in a regular W/Cu honeycomb with 20% W volume fraction, discretized with an 814x417-element mesh of quadrilaterals for homogenization using the Matlab script from [49].

Although this method is expedient, and particularly useful when the composite's microstructural topology itself will be optimized, it requires a very fine mesh to accurately represent the microstructure's geometry. For 2D domains with first-order elements, the required computational time is still insignificant. However, extension of this method to 3D produces a large number of degrees of freedom. This, combined with the use of higher-order elements for more accurate results, leads to long simulation times. Uniform, structured meshes were not used with *homog3d* for this reason.

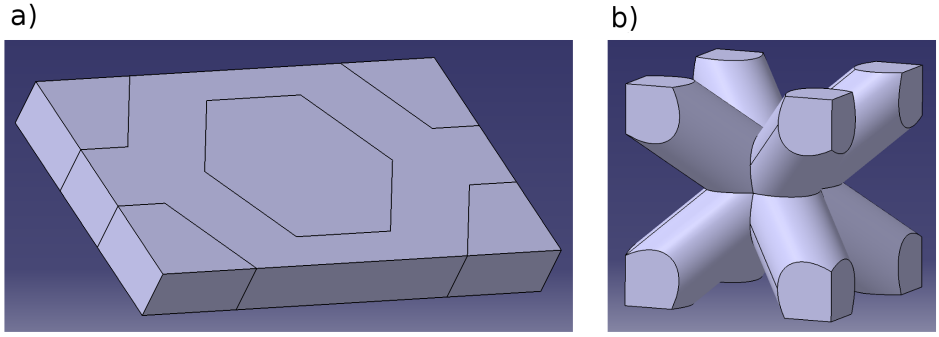

FIGURE 3.3: Multi-body parametric *CATIA* models of a) regular honeycomb RVE and b) BCC lattice RVE (matrix body hidden).

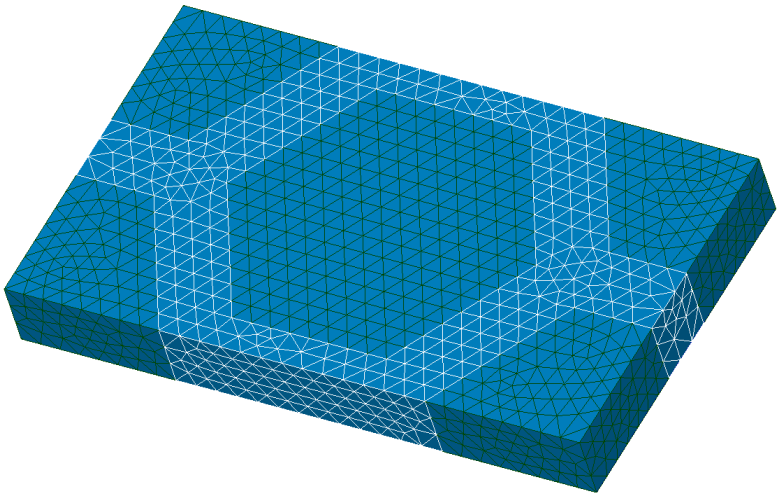

FIGURE 3.4: FE mesh of a regular honeycomb RVE.

Meshes used with *homog3d* are instead unstructured and composed of tetrahedra with quadratic interpolation (see Figure 3.4). Parametric CAD files created with *CATIA* (Figure 3.3) allow unit cells with a full range volume fractions and, for lattice structures, various lattice topologies to be created with minimal effort. The multi-body models were exported from *CATIA* in STEP format. The open-source pre- and post-processing platform *SALOME* was then used to generate tetrahedral meshes with the *Netgen* mesh generator. For an RVE modelled with 1mm characteristic size, meshes were created using an element edge length of 0.06mm. Meshes were transferred to *homog3d* in UNV format.

3.2 Homogenized properties of candidate microstructures

In order to create the desired two-variable material model, homogenized properties were calculated at multiple temperatures ranging from 20 to 1000°C. The tabulated temperature-dependent material properties in [64] were used for both CuCrZr and pure tungsten. Intermediate values were calculated with linear interpolation when necessary.

Since the properties of CuCrZr are generally insufficient for the alloy to be used at high temperatures without reinforcement, tabulated values are not available up to 1000°C. To create the material models for honeycomb and BCC lattices, the properties of CuCrZr were extrapolated by using the value at the highest tabulated temperature for all temperatures exceeding the tabulated range. Extrapolation to higher temperatures was performed to simplify implementation in the topology optimization code, since an extensive temperature range is necessary for regions near the surface of the tungsten armor. Until more realistic, experimental material models of W_{AM}/Cu composites exist, it is left to the designer to address composite regions with excessive temperatures in the subsequent detailed analysis following topology optimization.

The honeycomb RVE (Figure 3.3a) was parameterized with the ratio of cell wall thickness t to cell size w. Figure 3.5 shows the geometry of the unit cell and relevant dimensions.

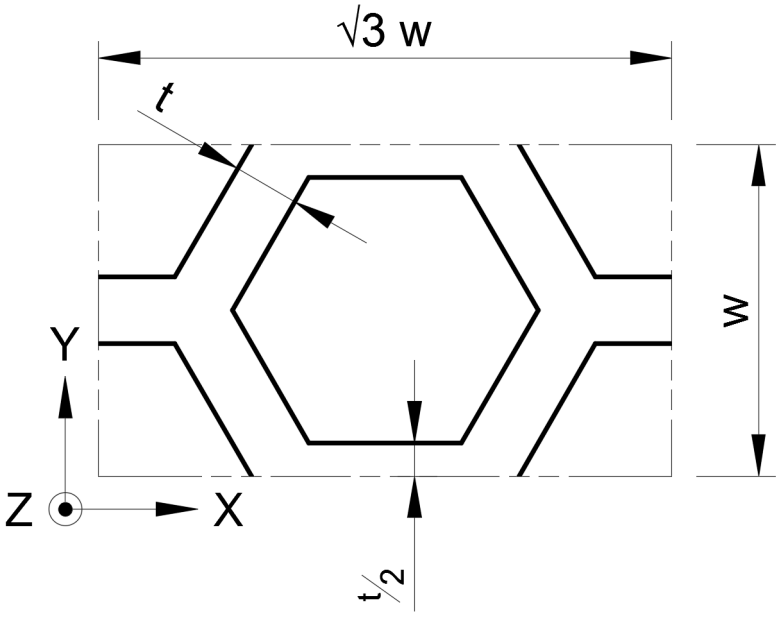

FIGURE 3.5: Dimensions of the regular honeycomb RVE.

The relationship between wall thickness and tungsten volume fraction (3.11) was determined geometrically.

$$V_{f,W} = 1 - \left(1 - \frac{t}{w}\right)^2 \tag{3.11}$$

The BCC lattice (Figure 3.3b) was parameterized with the ratio between the (uniform) diameter D_s of the struts and the side length of the RVE a. The relationship for the tungsten volume fraction was determined by fitting a cubic polynomial (3.12) to values measured in *CATIA*.

$$V_{f,W} = -4.89875\left(\frac{D_s}{a}\right)^3 + 5.44114\left(\frac{D_s}{a}\right)^2 + 6.12658(10^{-5})\left(\frac{D_s}{a}\right) \tag{3.12}$$
$$0 \leq \frac{D_s}{a} \lesssim 0.741$$

The properties of honeycomb are transversely isotropic: in-plane (XY) behavior is isotropic, but out-of-plane behavior differs somewhat. Properties of the BCC lattice are fully isotropic. Figure 3.6 compares the normal stiffnesses of the BCC lattice and honeycomb at an intermediate temperature of 400 °C to the analytical linear (ROM) and inverse (iROM) rule-of-mixtures models. The out-of-plane normal stiffness (E_z) of honeycomb follows linear ROM behavior.

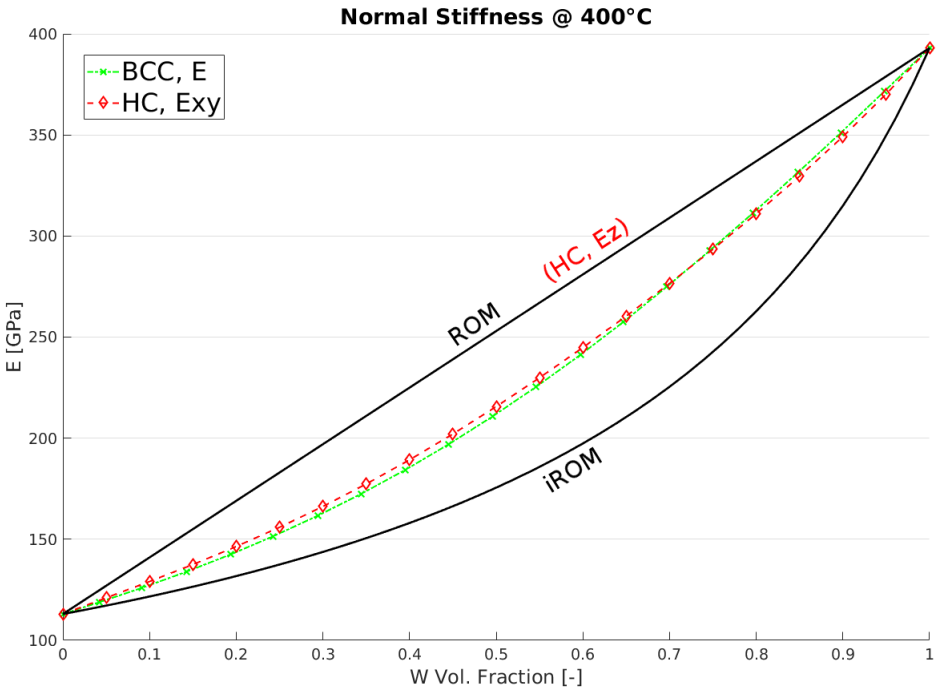

FIGURE 3.6: Comparison of normal stiffness at 400°C.

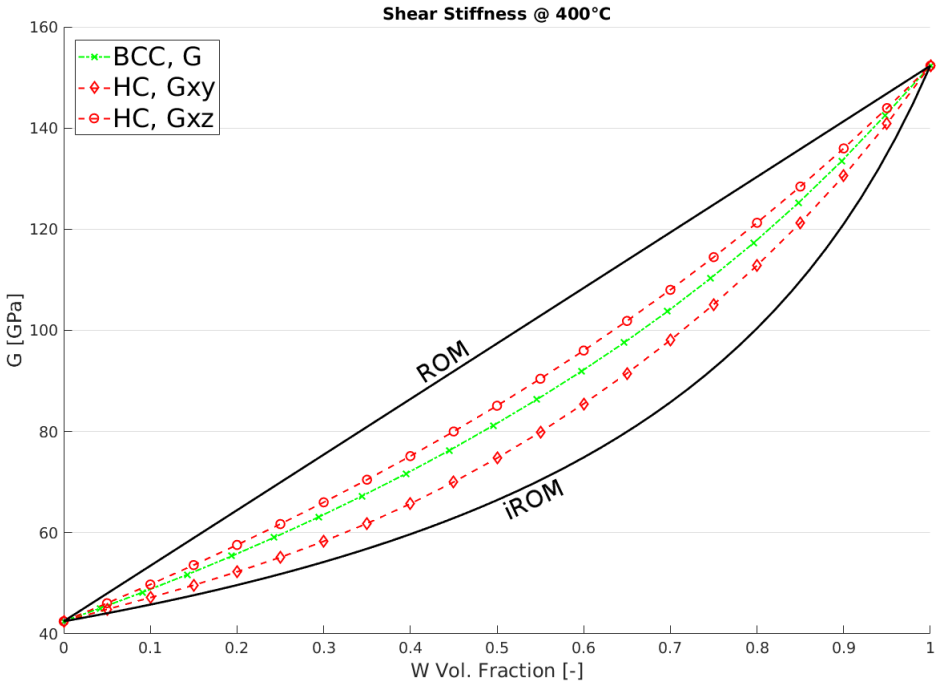

FIGURE 3.7: Comparison of shear stiffness at 400°C.

While the in-plane stiffness of honeycomb is very similar to that of the BCC lattice, linear ROM behavior makes honeycomb's E_z up to 20% higher for intermediate mixtures. Figure 3.7 visualizes the composites' shear stiffness in the same manner.

The comparison continues with Figure 3.8, showing the normal components of the thermal expansion tensor. Neither structure is fully anisotropic; shear components of thermal expansion are therefore zero. The in-plane isotropy of honeycomb seen for stiffness is also applicable to thermal expansion. The higher out-of-plane stiffness of the honeycomb also results in a decreased out-of-plane thermal expansion.

The relationships for thermal conductivity are shown in Figure 3.9. The highest thermal conductivity is achieved by honeycomb along its Z axis, which has linear ROM behavior. Since heat conduction in a PFC using this microstructure will largely be along the Z axis (see component model in Section 5.1), this feature should be advantageous.

Figure 3.10 depicts, as an example, the full two-variable model of normal stiffness for the BCC lattice. A step can be seen at 700°C, beyond which the properties of CuCrZr have been extrapolated as a constant.

The effect of the periodic boundary conditions can be seen by visualizing the

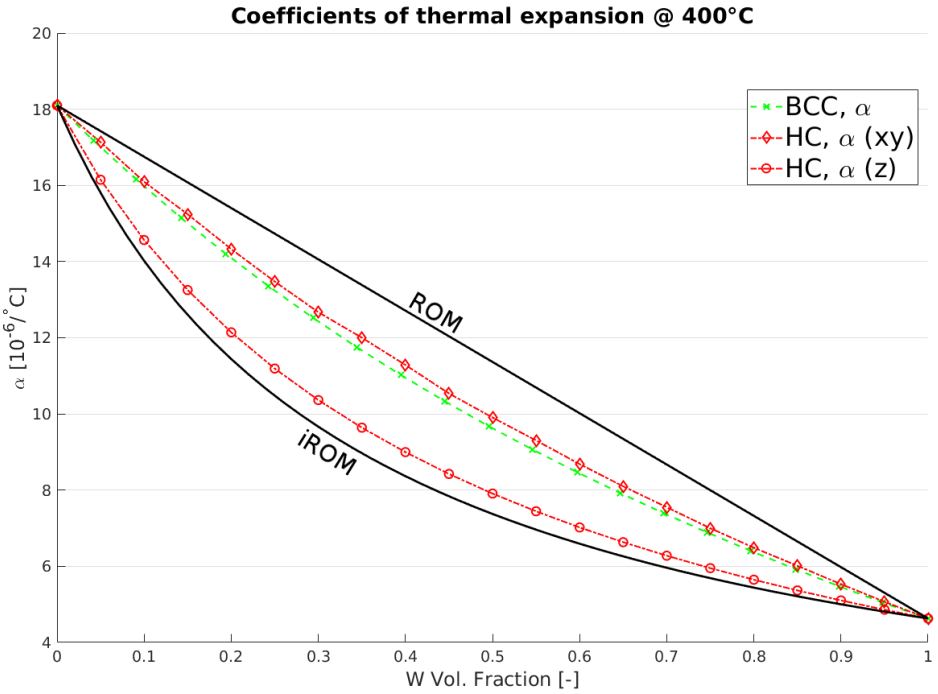

FIGURE 3.8: Comparison of thermal expansion at 400°C.

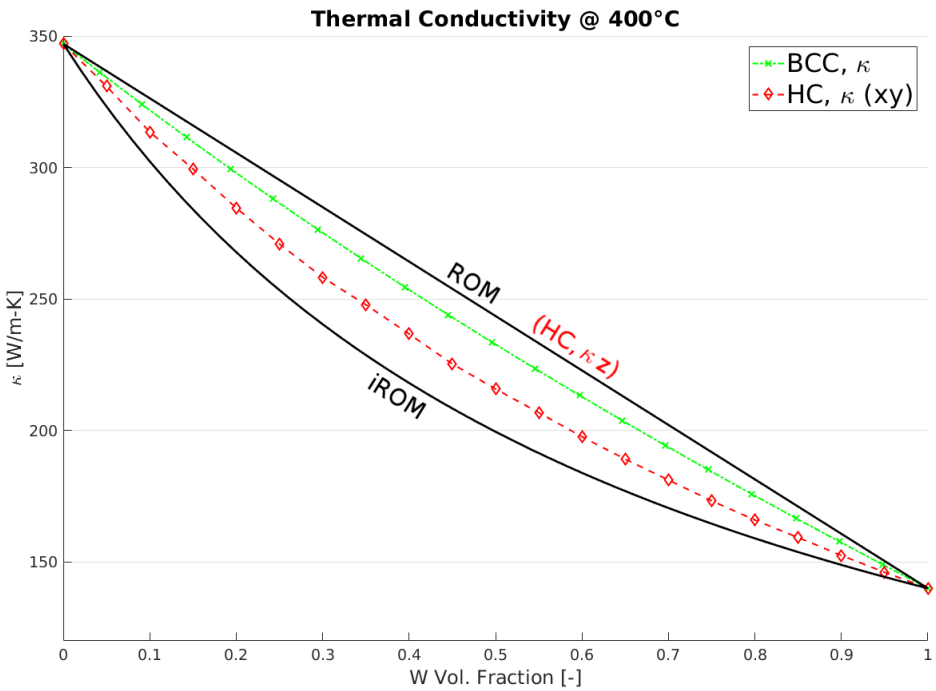

FIGURE 3.9: Comparison of thermal conductivity at 400°C.

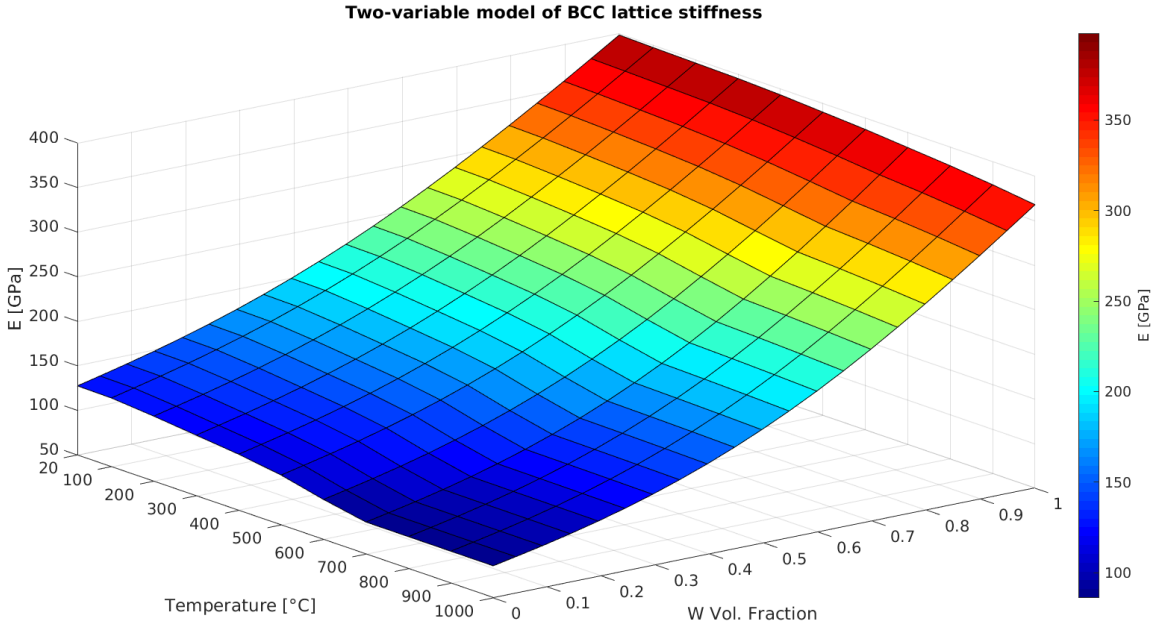

FIGURE 3.10: Two-variable plot of normal stiffness for the BCC lattice.

displacement field for a given strain load. Figure 3.11 shows the constrained expansion of a honeycomb RVE with 40% tungsten volume fraction when a temperature step of 1 °C is simulated to homogenize the microstructure's thermal expansion. Although the copper-alloy matrix experiences greater thermal strain due to its higher CTE, the much higher stiffness of the tungsten reinforcement allows it to swell relative to the matrix. Averaging of the internal stress response in this state is used to determine the thermoelastic tensor, and subsequently the thermal expansion tensor can be found.

The properties of neither structure are universally more suitable for stress reduction in PFCs. The isotropic CTE of the BCC lattice is nearly equal to the in-plane CTE of honeycomb. However, the even lower CTE and excellent thermal conductivity of honeycomb along its Z-axis may prove valuable. Ultimately, the effectiveness of a given microstructure can only be seen through optimization at the component level; microstructures with different properties may reduce stress to the same degree using different macroscopic material distributions.

Selection of a suitable microstructure requires consideration of manufacturability as well. The cross-section of a lattice consists of many small points, formed by thin struts which may be prone to breakage. Honeycomb has a high degree of interconnectivity within its cross-section and is much less fragile. However, removal of residual powder can only be performed from the end of a honeycomb cell due to its closed walls; the open structure of the BCC lattice allows

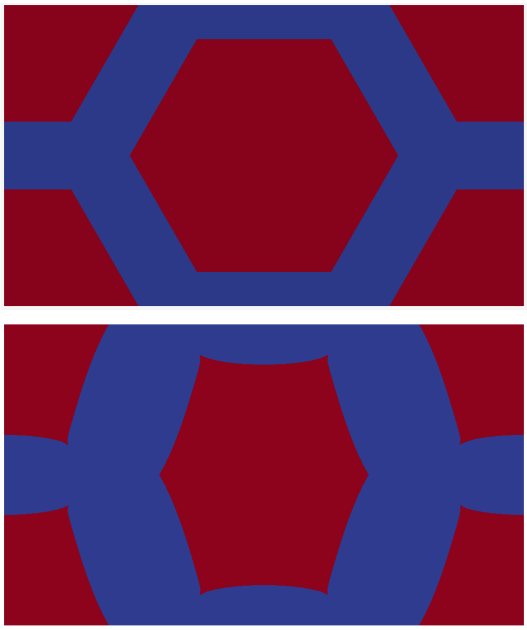

FIGURE 3.11: Internal displacement of a honeycomb RVE with 40% tungsten subjected to a temperature step to homogenize thermal expansion. Undeformed state (top), deformed state (bottom).

powder removal from all directions. Structural integrity, powder removal, and other practical aspects of producing tungsten microstructures with SLM must be assessed through testing.

Chapter 4

Topology optimization of plasma-facing components

The honeycomb and lattice structures characterized numerically in the previous chapter are examples of additively manufacturable composites that can be tailored locally to achieve the desired performance of a PFC. Here, the goal is stress reduction, but the interactions that produce thermal stresses are too complicated for the optimal structure to be predicted intuitively. A component-level topology optimization should therefore be used to achieve the greatest stress reduction.

This chapter presents the procedure to optimize the material distribution in a composite PFC to minimize stress under HHF loading. First, two potential mathematical formulations of this goal are described. Two variants of the algorithm are elaborated with a sensitivity analysis and implementation details: the simpler uses constant material properties (non-TD), and a more refined version considers the temperature-dependence of material properties (TD). The non-TD version was tested with a simple ROM material model, and the TD version with the two-variable models for regular honeycomb and a BCC lattice calculated by *homog3d*.

4.1 Formulation of the optimization problem

Selection of a suitable optimization problem requires consideration of multiple factors. Most importantly, all optimization objectives and constraints must be expressed mathematically; qualitative aspects of design must be considered separately. The ability to express the problem mathematically is, however, not sufficient on its own. Poor convergence behavior or excessive computational expense may disqualify certain approaches despite their conceptual suitability.

With that in mind, two formulations with objective functions based on the

von Mises equivalent stress were developed. For a 2D, plane-stress domain, the von Mises stress σ_V is calculated with (4.1) [65].

$$\sigma_V^2 = \sigma_1^2 + \sigma_2^2 - \sigma_1\sigma_2 + 3\tau_{12}^2 \tag{4.1}$$

This choice may seem to disregard the complexity of failure mechanisms in composite materials, especially those containing a brittle material like tungsten. However, it greatly simplifies implementation, and is justified by the following:

1. The von Mises stress is a good summary of the stress state, and is effective at reducing all components of stress during optimization.

2. Topology optimization is meant to enrich the design process, not to replace thorough analysis and validation of designs.

3. As discussed in Section 2.3.1, the lack of experimental data on the mechanical properties of SLM tungsten currently precludes realistic modelling of the failure mechanisms of W_{AM}/Cu composites.

The first formulation seeks to minimize the global stress metric (4.2), a discrete form similar to (2.17). This metric is the p-norm of the von Mises stress in the entire domain. Stress is evaluated at each of the n_{el} elements' n_{gp} integration points (ie. "Gauss" points):

$$\sigma_g = \left[\sum_{e=1}^{n_{el}}\sum_{g=1}^{n_{gp}}\left(\sigma_V^{(e,g)}\right)^p\right]^{\frac{1}{p}} \tag{4.2}$$

As p approaches ∞, the p-norm approximates the maximum of the summed values. The value of p should ideally be chosen as large as possible to best approximate the infinity norm. However, choosing a value too large will result in an overflow of the computer's finite numerical representation. A value of 100 yielded a reasonable approximation without numerical overflow using double-precision floating point arithmetic. Using larger values is possible, but produces only marginal returns.

In addition to the global stress objective function, the average volume fraction of tungsten ($V_{f,W}$) can be constrained to a maximum value if designs with more copper content are desired. The individual variable limits x^{min} and x^{max} provided by the standard MMA problem (2.18) can also be used to place a hard limit on local volume fractions. This is useful, for example, to ensure that the AM tungsten structure is open enough to remove unfused residual powder from the SLM process before melt infiltration.

Formulated with the global stress metric, the optimization problem is

$$\begin{aligned} \min \quad & \sigma_g \\ \text{subject to} \quad & \frac{1}{n}\sum_{j=1}^{n} x_j \leq \hat{V}_{f,W} \end{aligned} \tag{4.3}$$

The average volume fraction constraint is applied only to elements in the design domain. Translation of (4.3) to the standard MMA format is simple. The artificial variable z is unused, so a_0 is set to 1 and a_i is set to 0 for all other values of i. The variables y_i are used to traverse infeasible points; the coefficients c_i are set to a "large" value (10^3 was used) and the coefficients d_i to 1.

The second formulation treats stress locally. It uses the following "min-max" formulation:

$$\begin{aligned} \min \quad & z \\ \text{subject to} \quad & \bar{\sigma}_V^{(e)} \leq z, \qquad e = 1, \ldots, n_{el} \\ & \frac{1}{n}\sum_{j=1}^{n} x_j \leq \hat{V}_{f,W} \end{aligned} \tag{4.4}$$

Unlike the global formulation, (4.4) makes use of the artificial variable z provided by the standard MMA problem. This variable is minimized while the average von Mises stress in each element (4.5) is individually constrained to be less than or equal to z. The average von Mises stress $\bar{\sigma}_V^{(e)}$ in an element is found by averaging stress values over the element's n_{gp} integration points. Through the use of an artificial variable and local stress constraints, the algorithm indirectly minimizes the maximum von Mises stress observed in the domain.

$$\bar{\sigma}_V^{(e)} = \frac{1}{n_{gp}}\sum_{g=1}^{n_{gp}} \sigma_V^{(g)} \tag{4.5}$$

Since the artificial variable z becomes the objective function, f_0 is simply defined to be 0. The number of constraint functions m is equal to $n_{el} + 1$. All coefficients a_i are set to 1, except for the coefficient a_m corresponding to the average volume fraction constraint, which should be 0. The coefficients c_i and d_i are again set to 10^3 and 1, respectively.

4.2 Sensitivity analysis

The MMA, like most efficient algorithms for non-linear optimization, requires knowledge not only of the values of the system equations at the current solu-

tion point, but also of their derivatives. Thus, the derivative with respect to each design variable of the stress functions used in the optimization problems of the previous section must be calculated once per iteration. This process, known as sensitivity analysis, is illustrated in the following. This section assumes that material properties are independent of temperature. Section 4.2.1 extends the procedure for temperature-dependent material models.

The global stress metric (4.2) and element average von Mises stresses (4.5) are analytical functions of the local von Mises stress values at the integration points within the FE mesh. Their derivatives are calculated with (4.6) and (4.7) and are simple to evaluate once the derivatives of the local stress values are known.

$$\frac{\partial \sigma_g}{\partial \rho_j} = \frac{1}{p}\sigma_g^{1-p} \cdot \left[\sum_{e=1}^{n_{el}} \sum_{g=1}^{n_{gp}} p \left(\sigma_V^{(e,g)} \right)^{p-1} \cdot \frac{\partial \sigma_V}{\partial \rho_j}^{(e,g)} \right] \tag{4.6}$$

$$\frac{\partial \bar{\sigma}_V^{(e)}}{\partial \rho_j} = \frac{1}{n_{gp}} \sum_{g=1}^{n_{gp}} \frac{\partial \sigma_V}{\partial \rho_j}^{(g)} \tag{4.7}$$

Differentiation of the von Mises equivalent stress for 2D plane-stress domains (4.1) with respect to a design variable ρ_j leads to:

$$\begin{aligned} 2\sigma_V \left(\frac{\partial \sigma_V}{\partial \rho_j} \right) = 2\sigma_1 \left(\frac{\partial \sigma_1}{\partial \rho_j} \right) + 2\sigma_2 \left(\frac{\partial \sigma_2}{\partial \rho_j} \right) \\ - \sigma_1 \left(\frac{\partial \sigma_2}{\partial \rho_j} \right) - \left(\frac{\partial \sigma_1}{\partial \rho_j} \right) \sigma_2 + 6\tau_{12} \left(\frac{\partial \tau_{12}}{\partial \rho_j} \right) \end{aligned} \tag{4.8}$$

This requires knowledge of the current von Mises stress value as well as the components of the local stress tensor (A.11) and their derivatives. The derivative of the stress tensor within an element is calculated as follows:

$$\begin{aligned} \frac{\partial \boldsymbol{\sigma}^{(e)}}{\partial \rho_j} = \; & \mathcal{C} \left(\mathcal{B}^{(e)} \left(\frac{\partial \boldsymbol{d}^{(e)}}{\partial \rho_j} \right) - \boldsymbol{\alpha}^{(e)} (\boldsymbol{N}^{(e)})^T \left(\frac{\partial \boldsymbol{\theta}^{(e)}}{\partial \rho_j} \right) \right) + \\ & \delta_{je} \left[\left(\frac{\partial \mathcal{C}^{(e)}}{\partial \rho_e} \right) \left(\mathcal{B}^{(e)} \boldsymbol{d}^{(e)} - \boldsymbol{\alpha}^{(e)} (\boldsymbol{N}^{(e)})^T \Delta \boldsymbol{\theta}^{(e)} \right) - \cdots \right. \\ & \left. \mathcal{C} \left(\left(\frac{\partial \boldsymbol{\alpha}^{(e)}}{\partial \rho_e} \right) (\boldsymbol{N}^{(e)})^T \Delta \boldsymbol{\theta}^{(e)} \right) \right] \end{aligned} \tag{4.9}$$

The strain-displacement matrix $\mathcal{B}^{(e)}$ and element shape functions depend only on the FE formulation and the location of the integration points; they do not change with the design variables. The derivatives in the right-hand side of (4.9) take two forms: derivatives of the material properties $\mathcal{C}^{(e)}$ and $\boldsymbol{\alpha}^{(e)}$,

and derivatives of the discrete field variables $\boldsymbol{d}$ and $\boldsymbol{\theta}$. Since the material properties in an element depend only on the design variable assigned to that element, terms containing material property derivatives are zero for all but one of the design variables. This is indicated by the Kronecker delta δ_{je}. Changes due to the variable displacements and temperatures, however, are global and influence the stress in all elements. Derivatives of the temperature field are calculated directly with

$$\frac{\partial \boldsymbol{\theta}}{\partial \rho_j} = -\mathcal{K}_t^{-1} \left[\left(\frac{\partial \mathcal{K}_t}{\partial \rho_j} \right) \boldsymbol{\theta} \right] \tag{4.10}$$

The prescribed heat loads applied with $\boldsymbol{f_q}$ are constant and do not appear in the sensitivity analysis. It is clear that differentiating the temperature field requires an additional solution of the FE system for each derivative to be calculated. The computational expense of this process can be reduced significantly by saving the decomposed conductivity matrix from the original solution of $\boldsymbol{\theta}$. The matrix will therefore be decomposed only once per iteration of the optimizer; each subsequent load case requires only the much less time-consuming process of back-substitution. Differentiation of the static displacement field is performed in a similar manner.

$$\frac{\partial \boldsymbol{d}}{\partial \rho_j} = \mathcal{K}_s^{-1} \left[\frac{\partial \boldsymbol{f}}{\partial \rho_j} - \left(\frac{\partial \mathcal{K}_s}{\partial \rho_j} \right) \boldsymbol{d} \right] \tag{4.11}$$

As for the temperature field, evaluating these derivatives requires solving the FE system once for each design variable, but can be done efficiently by reusing the decomposed stiffness matrix from the original solution of $\boldsymbol{d}$. Since an element's conductivity and stiffness matrices $\mathcal{K}_t^{(e)}$ and $\mathcal{K}_s^{(e)}$ depend only on the element's own design variable, the sensitivities of the global system matrices require differentiation of only one element matrix per design variable:

$$\frac{\partial \mathcal{K}_t}{\partial \rho_j} = \sum_{e=1}^{n_{el}} \delta_{je} \frac{\partial \mathcal{K}_t^{(e)}}{\partial \rho_e} = h_z \int_{\Omega^{(j)}} \mathcal{F}^{(j)T} \left(\frac{\partial \kappa^{(j)}}{\partial \rho_j} \right) \mathcal{F}^{(j)} \, d\Omega \tag{4.12}$$

$$\frac{\partial \mathcal{K}_s}{\partial \rho_j} = \sum_{e=1}^{n_{el}} \delta_{je} \frac{\partial \mathcal{K}_s^{(e)}}{\partial \rho_e} = h_z \int_{\Omega^{(j)}} \mathcal{B}^{(j)T} \left(\frac{\partial \mathcal{C}^{(j)}}{\partial \rho_j} \right) \mathcal{B}^{(j)} \, d\Omega \tag{4.13}$$

Unlike in the thermal system, the load vector of the static problem $\boldsymbol{f}$ is not constant. This vector clearly depends on the changing temperature field. Differentiation of (A.21) produces

$$\frac{\partial \boldsymbol{f}^{(e)}}{\partial \rho_j} = \delta_{je} \left(\frac{\partial \mathcal{T}^{(e)}}{\partial \rho_e} \right) \Delta \boldsymbol{\theta}^{(e)} + \mathcal{T}^{(e)} \left(\frac{\partial \boldsymbol{\theta}^{(e)}}{\partial \rho_j} \right) \tag{4.14}$$

The matrix $\mathcal{T}^{(e)}$, like all element matrices, depends only on the element's own design variable:

$$\frac{\partial \mathcal{T}^{(e)}}{\partial \rho_e} = h_z \int_{\Omega^{(e)}} \mathcal{B}^{(e)^T} \left[\left(\frac{\partial \mathcal{C}^{(e)}}{\partial \rho_e} \right) \boldsymbol{\alpha}^{(e)} + \mathcal{C}^{(e)} \left(\frac{\partial \boldsymbol{\alpha}^{(e)}}{\partial \rho_e} \right) \right] \boldsymbol{N}^{(e)^T} d\Omega \tag{4.15}$$

The calculation of the temperature and displacement derivatives can be understood conceptually by viewing the square-bracketed quantities in (4.10) and (4.11) as pseudo-load vectors applied to the FE systems. A pseudo-load vector is built and the constrained system is solved once for each design variable. The resulting temperature or displacement field is the desired derivative.

The sensitivities of material properties depend on the method used to parameterize the material model. For a material model using linear ROM intepolation, sensitivities are constant, and can be evaluated as the difference between the properties for the composite's component materials. The derivative of the isotropic Young's modulus, for example, is simply

$$\frac{\partial E}{\partial \rho_j} = E_1 - E_0 \tag{4.16}$$

where E_1 and E_0 are the Young's moduli of the constituent materials represented by design variables 1.0 and 0.0 respectively.

4.2.1 Sensitivity analysis with temperature-dependent properties

Treatment of temperature-dependent properties requires that all derivatives of the previous section be transformed from partial to total derivatives. For the sensitivities of the stress objectives (4.6) and constraints (4.7), local von Mises stress (4.8), and local stress tensor (4.9), this requires only a change of notation, since the derivatives of these stress functions are calculated using the derivatives of their subsidiary terms.

An actual change of procedure is necessary for the derivatives of 1) material properties, and 2) the temperature and displacement fields. The first step is to calculate the partial derivative of the temperature field with (4.10). Sensitivities of material properties must then include a term to account for the change of temperature at the current integration point. The elasticity tensor, for example, is differentiated with

$$\frac{D\mathcal{C}^{(e)}}{D\rho_j} = \delta_{je} \frac{\partial \mathcal{C}^{(e)}}{\partial \rho_e} + \frac{\partial \mathcal{C}^{(e)}}{\partial T} \left(\boldsymbol{N}^{(e)^T} \frac{\partial \boldsymbol{\theta}^{(e)}}{\partial \rho_j} \right) \tag{4.17}$$

Total derivatives of the element conductivity and stiffness matrices are then built using

$$\frac{D\mathcal{K}_t^{(e)}}{D\rho_j} = h_z \int_{\Omega^{(e)}} \mathcal{F}^{(e)^T} \left(\frac{D\kappa^{(e)}}{D\rho_j} \right) \mathcal{F}^{(e)} \, d\Omega \tag{4.18}$$

$$\frac{D\mathcal{K}_s^{(e)}}{D\rho_j} = h_z \int_{\Omega^{(e)}} \mathcal{B}^{(e)^T} \left(\frac{D\mathcal{C}^{(e)}}{D\rho_j} \right) \mathcal{B}^{(e)} \, d\Omega \tag{4.19}$$

Note that, since the temperature field changes with each design variable, the material properties within an element no longer depend only on the design variable assigned to that element; changing a single variable alters properties in the entire domain. Finally, total derivatives of the temperature and displacement fields become

$$\frac{D\boldsymbol{\theta}}{D\rho_j} = -\mathcal{K}_t^{-1} \left[\left(\frac{D\mathcal{K}_t}{D\rho_j} \right) \boldsymbol{\theta} \right] \tag{4.20}$$

$$\frac{D\boldsymbol{d}}{D\rho_j} = \mathcal{K}_s^{-1} \left[\frac{D\boldsymbol{f}}{D\rho_j} - \left(\frac{D\mathcal{K}_s}{D\rho_j} \right) \boldsymbol{d} \right] \tag{4.21}$$

Between the use of (4.20) and (4.21), the total derivative of the element load vector $\boldsymbol{f}$ must be calculated with

$$\frac{D\boldsymbol{f}^{(e)}}{D\rho_j} = h_z \int_{\Omega^{(e)}} \mathcal{B}^{(e)^T} \left[\mathcal{C}^{(e)} \left(\frac{D\boldsymbol{\varepsilon}_{\boldsymbol{t}}^{(e)}}{D\rho_j} \right) + \left(\frac{D\mathcal{C}^{(e)}}{D\rho_j} \right) \boldsymbol{\varepsilon}_{\boldsymbol{t}}^{(e)} \right] d\Omega \tag{4.22}$$

using the sensitivity of the thermal strain within the element:

$$\begin{aligned} \frac{D\boldsymbol{\varepsilon}_{\boldsymbol{t}}^{(e)}}{D\rho_j} = \; & \boldsymbol{\alpha}_T^{(e)} \left(\boldsymbol{N}^{(e)^T} \frac{D\boldsymbol{\theta}^{(e)}}{D\rho_j} \right) + \frac{D\boldsymbol{\alpha}_T^{(e)}}{D\rho_j} \left(\boldsymbol{N}^{(e)^T} \boldsymbol{\theta}^{(e)} - 20°\mathrm{C} \right) \\ & - \delta_{je} \frac{\partial \boldsymbol{\alpha}_{T_0}^{(e)}}{\partial \rho_e} \left(T_0 - 20°\mathrm{C} \right) \end{aligned} \tag{4.23}$$

Finally, the total derivative of the stress tensor forms the link to the stress objective/constraints:

$$\frac{D\boldsymbol{\sigma}^{(e)}}{D\rho_j} = \frac{D\mathcal{C}^{(e)}}{D\rho_j} \left(\mathcal{B}^{(e)} \boldsymbol{d}^{(e)} - \boldsymbol{\varepsilon}_{\boldsymbol{t}}^{(e)} \right) + \mathcal{C}^{(e)} \left(\mathcal{B}^{(e)} \frac{D\boldsymbol{d}^{(e)}}{D\rho_j} - \frac{D\boldsymbol{\varepsilon}_{\boldsymbol{t}}^{(e)}}{D\rho_j} \right) \tag{4.24}$$

4.3 Implementation

The cross-section shown in Figure 4.1 was used to demonstrate the optimization formulation described in the previous sections. The dimensions are typical of ITER-like PFC designs. A 5mm region facing the plasma was fixed to be pure tungsten to ensure a minimum thickness of armor material. The rest of the component comprises the design domain, where the W/Cu mixture may vary freely. A steady-state heat flux Q_N is applied at the surface of the tungsten armor. Convection in the cooling channel was simplfied to a uniform surface temperature of 150°C. Because of the domain's symmetry, only half of

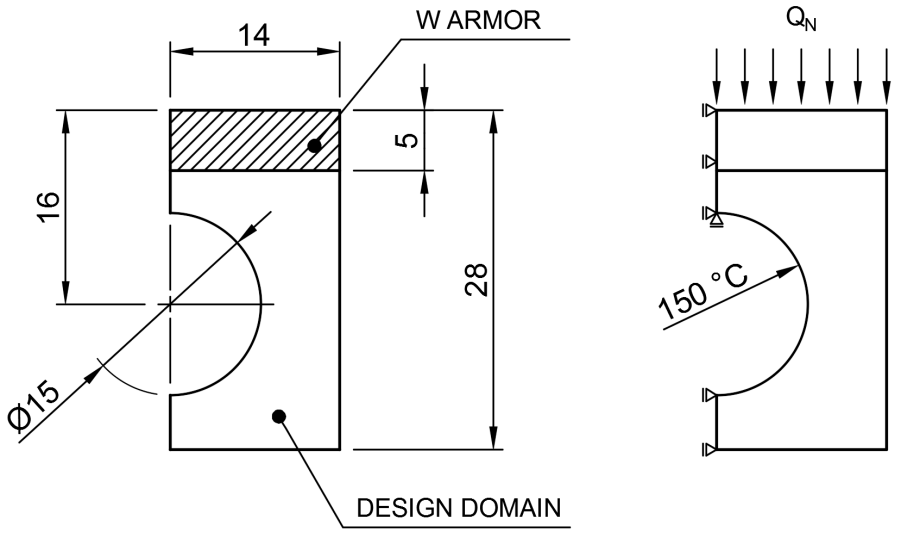

FIGURE 4.1: Dimensions and boundary conditions of the optimized component.

the component was simulated.

The temperature and displacement fields are discretized with 4-node quadrilaterals using bilinear interpolation of the primary variables. Linear-elastic material behavior is assumed. Meshes were generated procedurally as a grid, with elements in the cooling channel removed (Figure 4.2). This simplifies post-processing of the results, but unstructured meshes can be used as well. The stepped representation of the cooling channel surface complicates the use of convection boundary conditions; an unstructured mesh with a smooth cooling channel surface is therefore preferred when a convection model is to be used.

The von Mises stress within each element (4.5) is averaged across 4 integration points. Because the material distribution in the design domain varies between two solid materials – no void regions develop – the stress singularities that afflict most topology optimization problems do not occur; treatments such as "ϵ-relaxation" are unnecessary.

To reduce calculation time, sensitivities are calculated only for design variables associated with elements in the design domain; elements in the armor region fixed to tungsten are skipped. Filtering of sensitivities with (2.16) was tested using the weighting function

$$w(\boldsymbol{x}_e) = \begin{cases} 1 - \frac{\|\boldsymbol{x}_e - \boldsymbol{x}_0\|}{\hat{R}_f} & \|\boldsymbol{x}_e - \boldsymbol{x}_0\| \leq \hat{R}_f \\ 0 & \|\boldsymbol{x}_e - \boldsymbol{x}_0\| > \hat{R}_f \end{cases} \tag{4.25}$$

where the vector magnitude is the distance between the centroid of the summed element ($\boldsymbol{x}_e$) and the central element ($\boldsymbol{x}_0$) for which the updated sensitivity

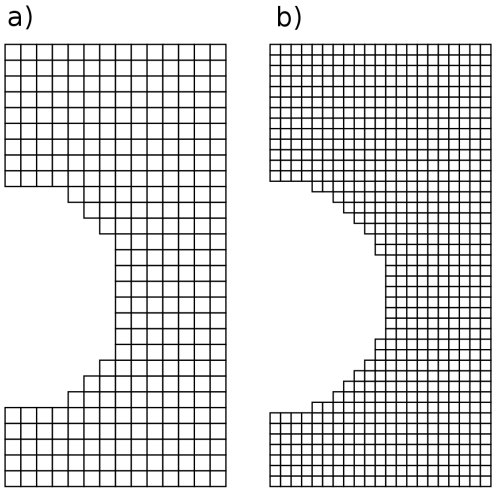

FIGURE 4.2: Gridded meshes of the optimized component with a) 14x28 and b) 21x42 elements.

is being calculated. The filter radius $\hat{R}_f$ should be at least large enough that the weighting function encompasses the central element's immediate neighbors.

In order to demonstrate the versatility of the methodology and better understand the factors that influence the resulting topology, optimizations were performed with multiple load cases. Two parameters define a load case: the nominal heat flux from the plasma Q_N and the reference temperature for thermal expansion T_0. Heat flux was varied to show how components can be adapted to diverse reactor operating conditions and to the various heat loads present in a single reactor. The effect of the reference temperature T_0 was investigated due to uncertainty concerning its actual value for W_{AM}/Cu composites. The temperature at which melt-infiltrated W/Cu composites are mostly free of thermal strains is generally unknown. This property depends on manufacturing, heat treatment, and thermal cycling history. Until the strain state of these composites is better understood, the principal goal is to characterize trends and the sensitivity of a component design to deviations of T_0. A combination of 4 nominal heat fluxes and 5 reference temperatures, shown in Table 4.1, required simulating 20 load cases.

$Q_N =$	5	10	15	20		[MW/m^2]
$T_0 =$	150	400	650	900	1150	[°C]

TABLE 4.1: Parameter set defining load cases. Q_N is the nominal heat load applied to the component, and T_0 is the reference temperature for thermal expansion.

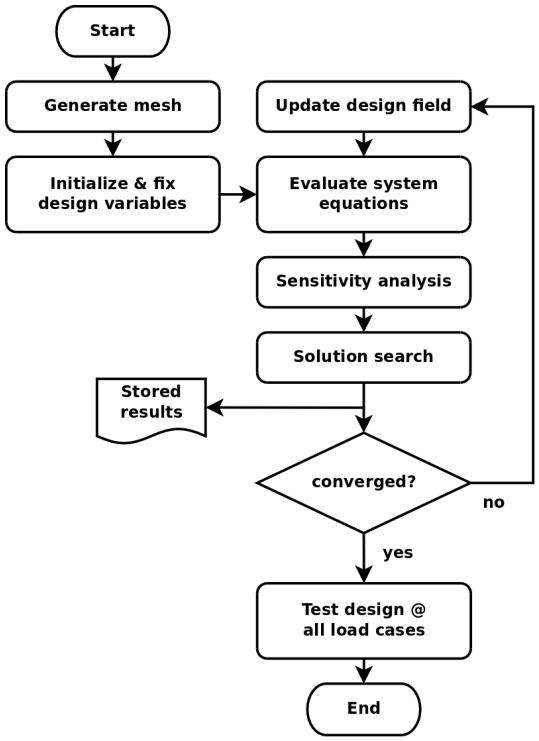

FIGURE 4.3: Flow chart of the optimization algorithm.

After optimization for a particular load case, stress in the optimized component was additionally measured using the parameters from all other load cases to examine its behavior when subjected to off-nominal conditions.

Figure 4.3 describes the procedure of a typical optimization. Convergence is achieved when the objective function and design variables have stabilized, and the solution satisfies all constraints. Each of these three conditions has its own tolerance. For stress objectives, 1 - 2 MPa is reasonable. For design variables and constraints, 10^{-2} was used. Minor, localized oscillation of stress or design variables may prevent convergence to these tolerances even after the structure as a whole no longer experiences major changes. To avoid this, the optimization may also be constrained to a maximum number of iterations.

A simple linear ROM material model was used to test the *TopOpt* code without temperature-dependent material properties. Properties at an intermediate temperature of 500°C were used for both materials (see Table 4.2). Temperature-dependent material properties were calculated with the two-variable models produced by *homog3d* for honeycomb and BCC lattices. Values between tabulated points were found with bilinear interpolation.

Material	E [GPa]	ν [-]	α [K^{-1}]	κ [W/(m K)]
W	390	0.29	4.89×10^{-6}	133
CuCrZr	106	0.33	19.55×10^{-6}	346

TABLE 4.2: Young's modulus, Poisson ratio, CTE, and thermal conductivity of W and CuCrZr at 500°C [64].

With the addition of temperature-dependent material properties, the thermal conduction problem becomes nonlinear. This was handled by solving the thermal problem iteratively, using the latest temperature field to calculate material properties for each new solution until the temperature field stabilizes. Iteration ends after the maximum nodal temperature change is below 0.1°C. The temperature field is initialized to a uniform 400°C at the beginning of the optimization. Subsequent iterations of the optimization algorithm start from the final temperature field of the previous iteration.

The sensitivity analysis for temperature-dependent optimization was tested in two forms. In unmodified form, as presented in Section 4.2.1, sensitivities are calculated using total derivatives of the material properties. In this case, contributions from *every* element must be assembled into the pseudo-load vectors applied to the system, and differentiation of the temperature field must be performed twice – once as a partial derivative, and then as a total derivative. This increases the computational complexity substantially. Since the temperature-dependence of the material properties in an element is much weaker than their dependence on the local design variable, an alternative form was tested, whereby properties are evaluated at the current local temperature, but the partial derivative with respect to temperature is assumed to be zero. This allows the use of partial derivatives with respect to the local design variable as a substitute for total derivatives, which reduces computation time and likely has little effect on the end result.

4.4 Results

This section presents the results of numerous tests performed with the *TopOpt* code. The purpose is to illustrate the capabilities and characteristics of the presented optimization approach. Emphasis is placed on understanding the interactions between the numerous parameters that influence the optimal design. Numerical behavior of the algorithm is also discussed.

The reference configuration to which optimized material distributions are compared is a full-tungsten gridded mesh (as in Figure 4.2). Although this isn't

entirely representative of real, contemporary PFC designs, it is useful for comparing various approaches and understanding the behavior of the algorithm. In Chapter 5, sample optimized designs are compared with realistic traditional designs. Table 4.3 shows the peak von Mises stress for the reference configuration at each heat load.

Q_N [MW/m^2]	5	10	15	20
σ_{max} [MPa]	260.5	576.1	922.5	1264.2

TABLE 4.3: Maximum von Mises stress in a full-tungsten domain at tested heat loads.

Figure 4.4 visualizes the stress and temperature fields in the full-tungsten domain at 15 MW/m^2. The fields at other heat loads are similar, but vary in intensity. Material distributions are depicted in the following images using a white-blue color scale, with copper alloy represented as white and tungsten as blue. The various shades of blue representing intermediate composite mixtures thus darken with increasing tungsten content.

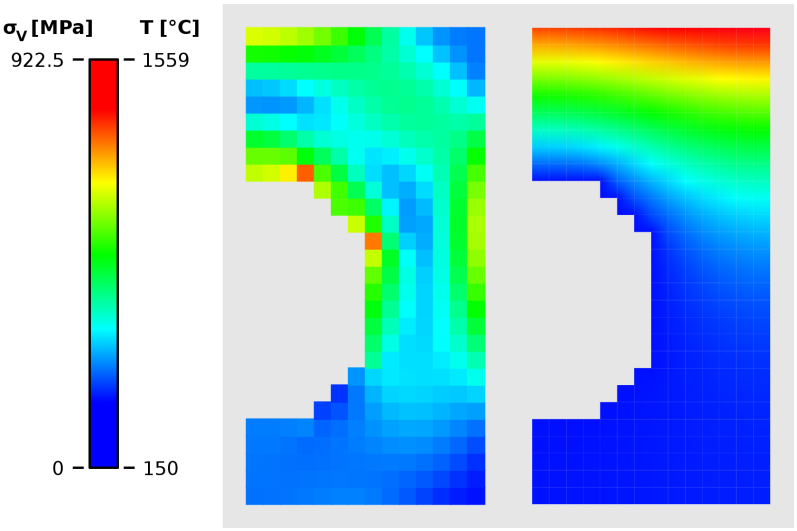

FIGURE 4.4: Stress (left) and temperature (right) in the reference component with a heat load of 15 MW/m^2.

Both formulations from Section 4.1 were initially tested with the non-TD ROM model. The local formulation (4.4) reliably yields stress reductions and manufacturable material distributions. Its main disadvantage is the time required for computation, due to the large number of local stress constraint functions. Only two functions must be evaluated for the global formulation (4.3), so this

approach is noticeably quicker. However, the global formulation does not reliably produce usable results. In fact, the global formulation occasionally yields a stress *increase*. Optimizing a component for a heat load of 5 MW/m^2 and a reference temperature of 900°C (referred to as the 5/900 load case) results in an increase of stress of over 150% after 50 iterations, for example. While there are cases where the global formulation does outperform the local formulation numerically, many of these results are impractical. The component in Figure 4.5 was optimized for the 15/400 load case, but the discrete tungsten feature encompassing the cooling channel would be effectively impossible to realize. Because of its robustness and good results, the local formulation is suggested and is investigated in detail in the following.

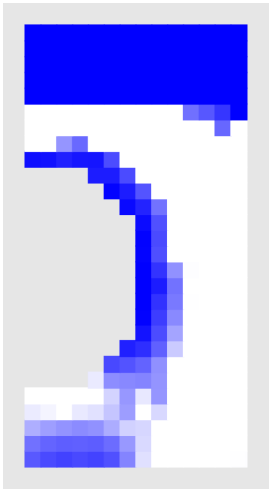

FIGURE 4.5: Material distribution of a component optimized for the 15/400 load case with the global formulation and non-TD ROM material model.

The parameters Q_N and T_0 influence the optimal design significantly. Figure 4.6 shows the optimized material distribution for all 20 load cases using a BCC lattice structure. The initial material distribution was a full-tungsten domain. The results exhibit common features that help deduce the means of stress reduction qualitatively. The copper-dense region that develops on the unconstrained sides, for example, lends the structure a degree of compliance at the free surface that likely reduces stress at the armor/heat-sink interface. The interaction between Q_N and T_0 is also visible. A concurrent increase of both parameters changes the optimal material distribution only negligibly. For example, the material distributions in Figure 4.5 for the 10/650 and 15/900 load cases appear nearly identical. A greater heat flux results in higher temperatures; it's logical to expect that thermal expansion in a given structure is reduced by increasing the reference temperature to better match actual temperatures in the component.

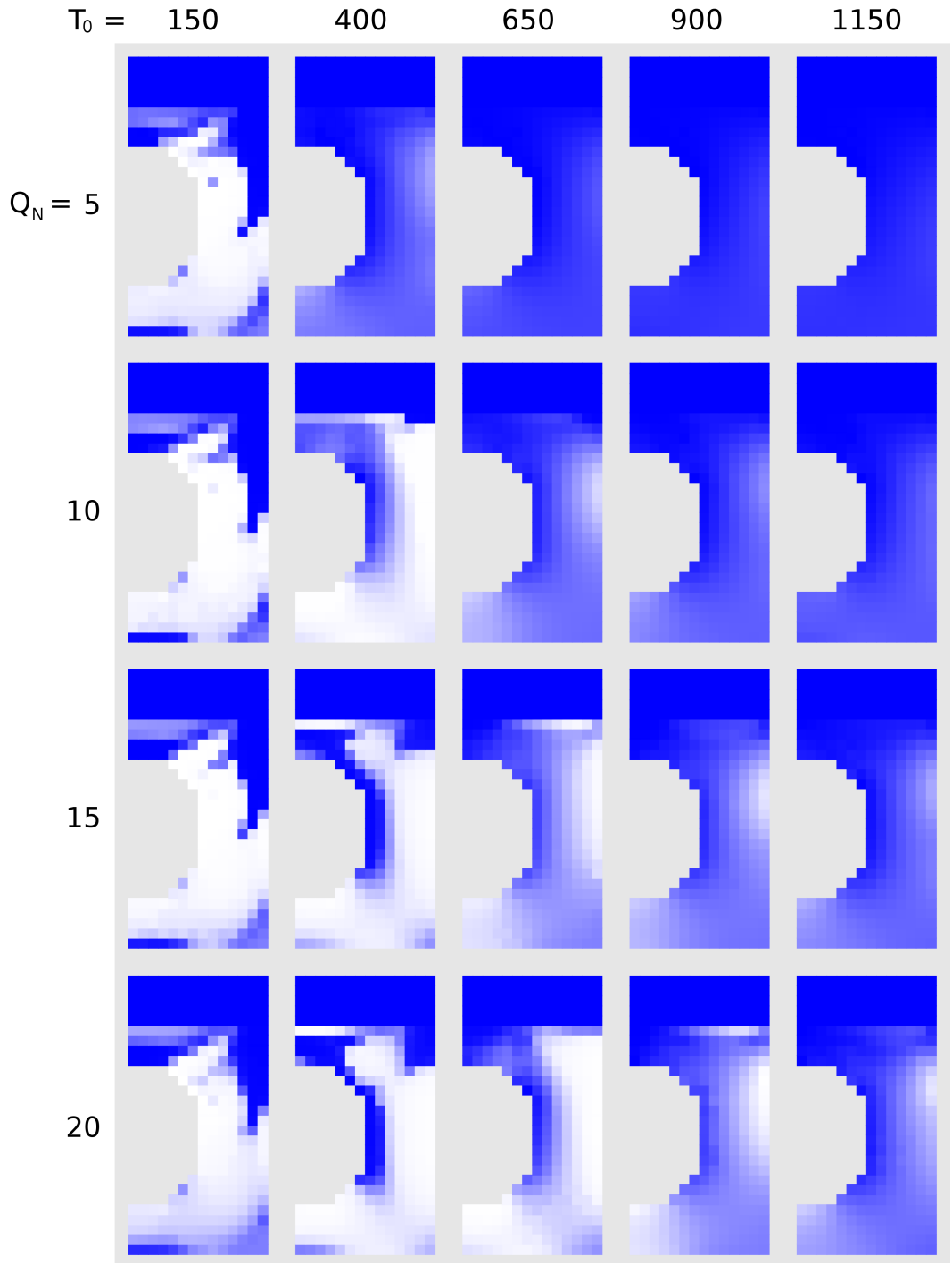

FIGURE 4.6: Influence of parameters Q_N (in MW/m^2) and T_0 (in °C) on the resulting material distribution with a BCC lattice material model. Blue indicates tungsten, white copper.

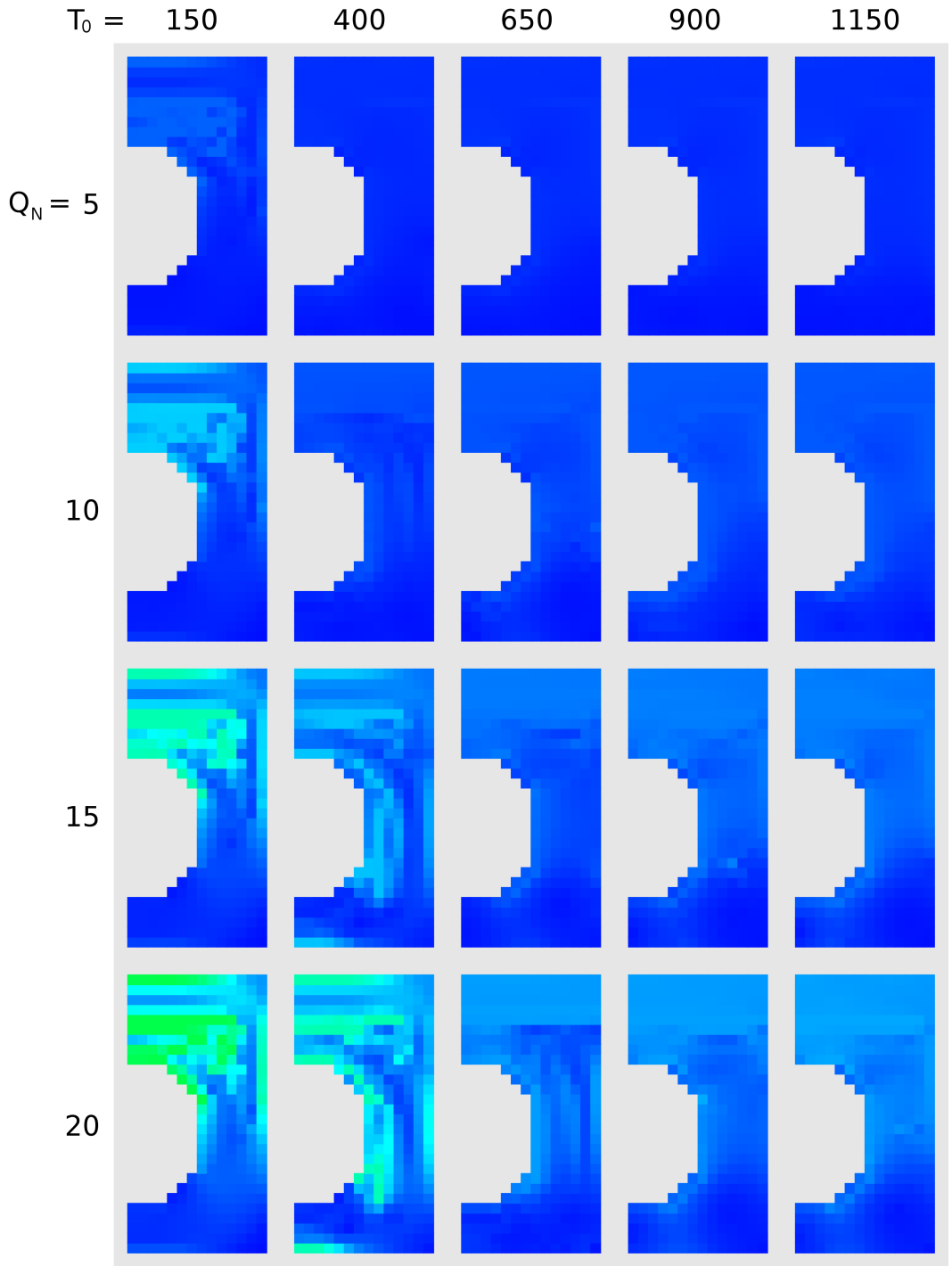

FIGURE 4.7: Visualization of stress in optimal designs with a BCC lattice for various values of Q_N (in MW/m^2) and T_0 (in °C). Regions of dark blue indicate low stress. Color changes to light blue, then light green for increasing stress.

Q_N [$\frac{\mathrm{MW}}{\mathrm{m}^2}$]	T_0 [°C]	σ_{max} [MPa]	Rel. $\Delta\sigma_{max}$	Final $V_{f,W}$
5	150	98.2	-62.3%	0.342
5	400	42.9	-83.5%	0.696
5	650	41.8	-84.0%	0.828
5	900	42.6	-83.6%	0.866
5	1150	41.6	-84.0%	0.876
10	150	219.1	-62.0%	0.315
10	400	84.9	-85.3%	0.245
10	650	82.2	-85.7%	0.605
10	900	87.2	-84.9%	0.729
10	1150	88.4	-84.7%	0.776
15	150	355.5	-61.5%	0.307
15	400	177.9	-80.7%	0.295
15	650	124.8	-86.5%	0.399
15	900	139.7	-84.9%	0.583
15	1150	139.9	-84.8%	0.689
20	150	479.2	-62.1%	0.341
20	400	370.4	-70.7%	0.286
20	650	177.1	-86.0%	0.285
20	900	185.6	-85.3%	0.454
20	1150	198.8	-84.3%	0.606

TABLE 4.4: Maximum stress, stress reduction, and final average volume fraction for structures optimized with a BCC lattice.

Table 4.4 shows the quantitative results of optimization with a BCC lattice. The predicted stress reduction is significant, roughly 85% for the majority of cases. Though the local formulation is effective at reducing stress for all load cases, the improvement is generally less pronounced for low values of T_0, since higher values better match the actual temperatures within the component.

Figure 4.8 shows selected iterations of an optimization for the 10/650 load case with a BCC lattice to demonstrate the efficiency with which the optimization algorithm achieves stress reduction. Within 3 iterations, the peak stress has

already decreased by 76.9%, and the developing structure is visible. After 10 - 15 iterations, the material distribution and stress field have largely stabilized.

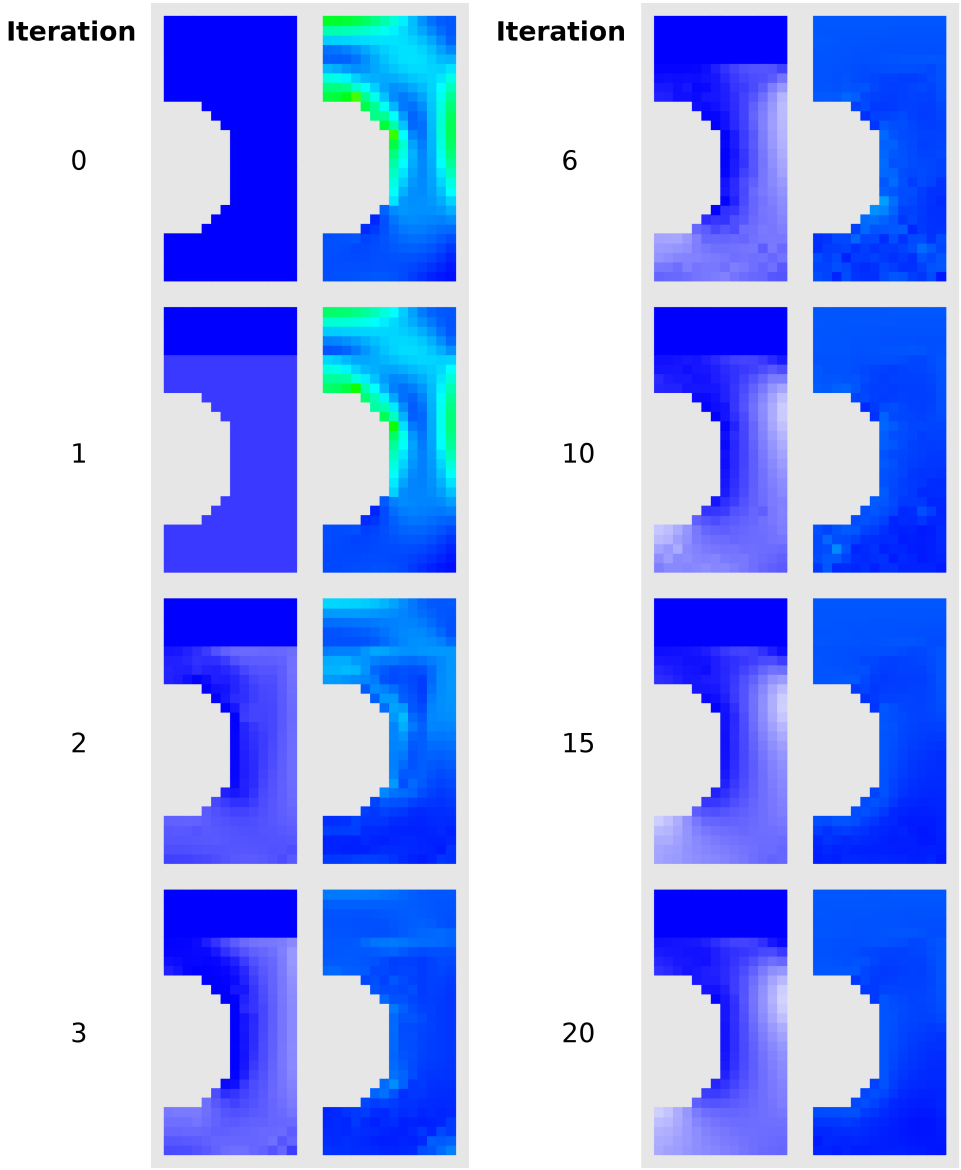

FIGURE 4.8: A sequence showing the progress of the optimization for the 10/650 load case with a BCC lattice. Each pair of images displays the material distribution (left) and the stress field (right).

Components optimized for a specific load case experience higher stresses when subjected to off-nominal conditions. The maximum stress in a BCC component optimized for the 10/650 load case was calculated assuming off-nominal heat loads and reference temperatures (Table 4.5). The fourth and fifth columns compare the maximum stress to, respectively, the value measured for nominal

conditions and the stress in the reference configuration at the considered heat load. An increase of maximum stress is evident, but the final column shows that, in most cases, the optimized design is still an improvement over the reference configuration at off-nominal conditions.

Q_N $[\frac{\mathrm{MW}}{\mathrm{m}^2}]$	T_0 [°C]	σ_{max} [MPa]	$\sigma_{max}/\sigma_{nom}$	$\sigma_{max}/\sigma_{ref}$
5	150	248.7	303%	95%
5	400	56.9	69%	22%
5	650	248.9	303%	96%
5	900	485.7	591%	186%
5	1150	734.5	894%	282%
10	150	538.1	655%	93%
10	400	280.4	341%	49%
10	650	82.2	100%	14%
10	900	229.4	279%	40%
10	1150	446.1	543%	77%
15	150	854.5	1040%	93%
15	400	598.5	728%	65%
15	650	365.7	445%	40%
15	900	141.3	172%	15%
15	1150	222.1	270%	24%
20	150	1167.1	1420%	92%
20	400	911.9	1110%	72%
20	650	679.4	827%	54%
20	900	447.2	544%	35%
20	1150	205.7	250%	16%

TABLE 4.5: Stress in a BCC component optimized for the 10/650 load case assuming off-nominal conditions.

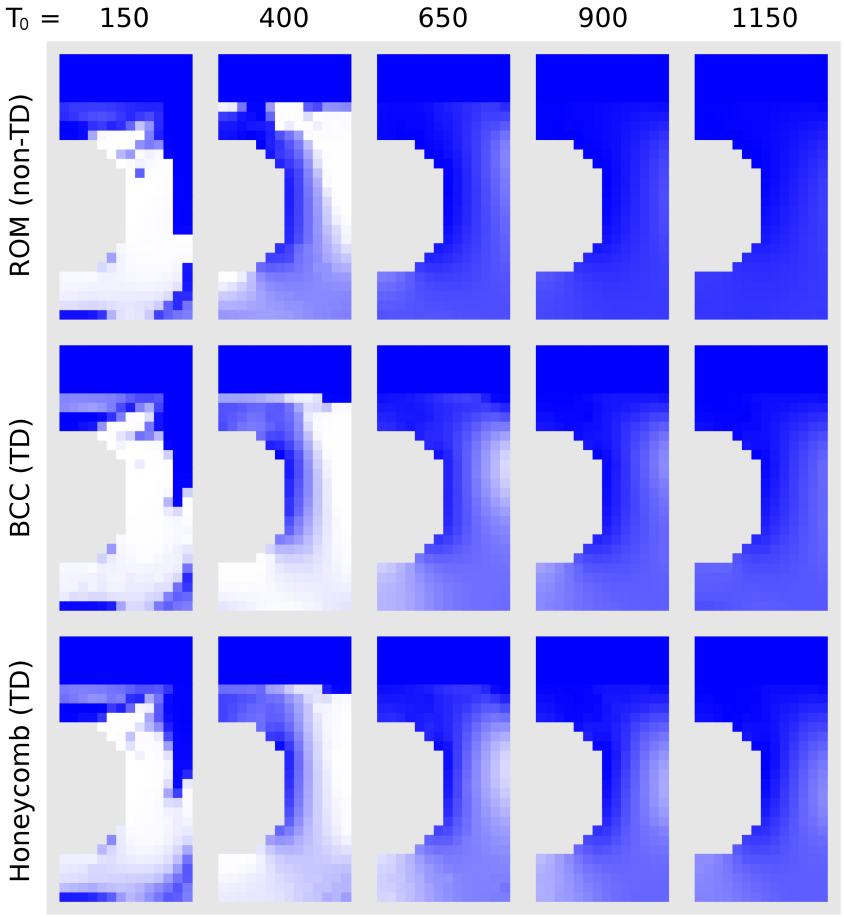

FIGURE 4.9: Comparison of material models with a heat load of 10 MW/m^2.

Figure 4.9 shows a comparison of results at 10 MW/m^2 using three different material models. Both temperature-dependent models (BCC lattice and honeycomb) produce similar results. The non-TD ROM model, however, results in material distributions that are slightly different from those produced with TD models. Table 4.6 compares the maximum stress in the components shown in Figure 4.9. Stress in the designs optimized using the non-TD ROM model was calculated additionally with both TD models to permit a realistic comparison with the BCC and honeycomb structures. In all cases, non-TD ROM material distributions exhibit an increase of maximum stress when simulated using the more realistic temperature-dependent properties. This effect is most significant for higher values of T_0.

As discussed in Section 4.2.1, the temperature-dependent sensitivity analysis formally requires the use of total derivatives that consider the changing temperature at each integration point, since the material properties within an element are coupled to all design variables in the domain via the temperature field. However, the contribution of temperature dependence to total deriva-

T_0 [°C]	ROM (a)	ROM (b)	ROM (c)	BCC	Honeycomb
150	224.2	240.1	232.0	219.1	226.2
400	117.2	126.1	131.1	84.9	73.0
650	99.2	260.2	337.9	82.2	79.7
900	110.6	294.4	364.0	87.2	79.2
1150	101.6	300.2	369.6	88.4	87.2

TABLE 4.6: Comparison of maximum stress (in MPa) in designs optimized for 10 MW/m^2 with various material models. Stress in the ROM designs was evaluated with a) the non-TD ROM model, b) the TD BCC model, and c) the TD honeycomb model.

tives within an element (e.g. Equation 4.17) is negligibly small for two reasons: First, the partial derivative of material properties with respect to the local design variable is generally $10^3 - 10^5$ times larger than the partial derivative with respect to temperature. Second, a single element's design variable only has a small effect on the temperature field as a whole.

Temperature-dependent optimization with and without the use of total derivatives was tested on the 10/650 load case with the BCC material model. The maximum stress in the optimized design varied by less than 2 MPa, and there was no significant difference in the optimal material distributions. However, because of the extra effort required to calculate the total derivatives, their use more than doubled the computation time. Since this disadvantage was not balanced by any practical benefit, partial derivatives were used as a substitute for the presented results.

The composite mixture is unconstrained in the previous material distributions; the full range of volume fractions was allowed. It was mentioned in Section 4.1 that restricting the range of allowable design variables can be used to exclude dense microstructures that hamper powder removal and melt-infiltration. Figure 4.10 shows the material distributions that result when design variables are restricted everywhere to a maximum of 0.5, 0.7, and 1.0 (from left to right) for the 10/650 load case. The material distributions are qualitatively very similar. The stress-reduction achieved when constraining the local volume fraction is different than the unrestricted solution, however. Table 4.7 shows maximum stress values corresponding to Figure 4.10 and the reduction relative to the reference value for 10 MW/m^2. Restricting the solution space naturally results in an increase of stress compared to the unrestricted optimum. However, the stress reduction of the constrained designs is still substantial.

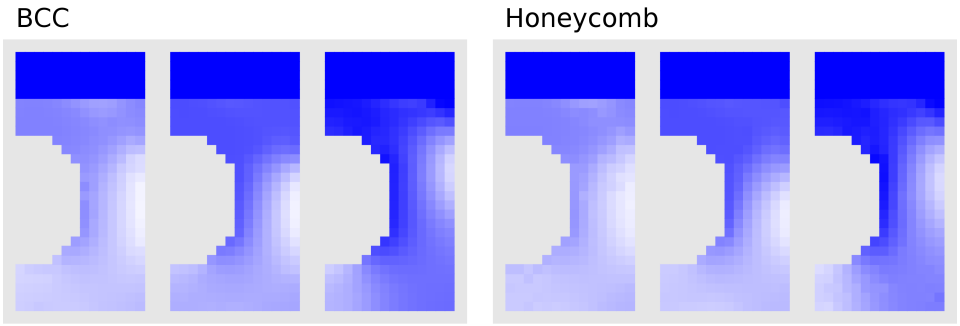

FIGURE 4.10: Structures optimized for the 10/650 load case with locally constrained composite volume fraction. From left to right for each microstructure: maximum volume fraction of 0.5, 0.7, and 1.0.

	BCC			Honeycomb		
Max. $V_{f,W}$	0.5	0.7	1.0	0.5	0.7	1.0
σ_{max} [MPa]	239.3	145.7	82.2	266.6	145.1	79.7
Rel. $\Delta\sigma_{max}$	-58.5%	-74.7%	-85.7%	-53.7%	-74.8%	-86.2%

TABLE 4.7: Maximum stress and relative stress reduction for components optimized for the 10/650 load case with locally constrained volume fraction.

Though constraining the global average volume fraction is implemented in the formulation of the optimization problem, testing did not demonstrate noteworthy advantages. This method is not effective at preventing dense structures (to aid manufacturing) and results in higher levels of stress than unconstrained material distributions.

The BCC component was optimized for 10 MW/m^2 using multiple initial material distributions in order to evaluate the influence of the optimization problem's non-convexity. Figure 4.11 compares optimized designs that began with uniform distributions of tungsten and copper, respectively. It is clear that the initial distribution can bias the average volume fraction of the optimal solution: optimizations that started with a full-copper domain typically produce optimal structures with higher copper content. Table 4.8 shows this effect quantitatively, as well as the maximum stress and stress reduction in each solution. Although it's clear that the choice of initial distribution may impede the algorithm's ability to find particular solutions, and that the solutions are certainly local optima, achieving a substantial stress reduction is itself not inhibited.

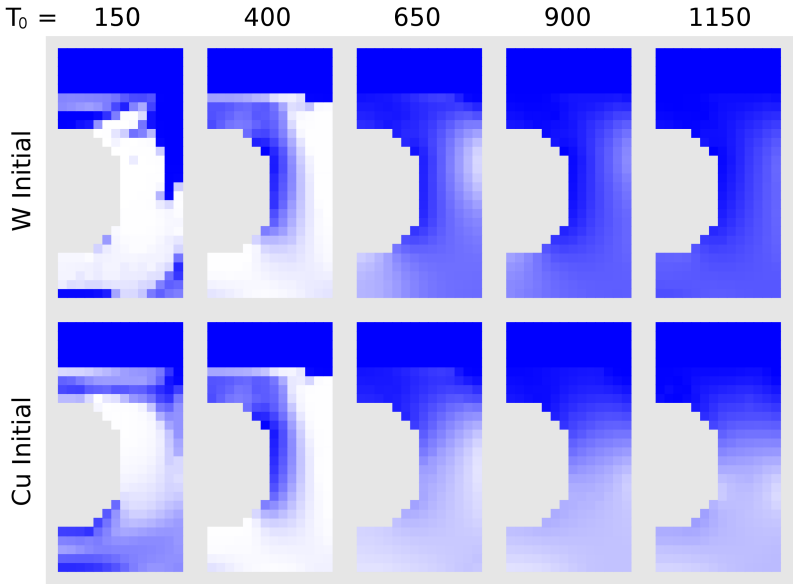

FIGURE 4.11: BCC component optimized for 10 MW/m^2 with different initial distributions. Design variables were initially 1.0 (top) and 0.0 (bottom).

Initial $V_{f,W}$	T_0	σ_{max} [MPa]	Rel. $\Delta\sigma_{max}$	Final $V_{f,W}$
1.0	150	219.1	-62.0%	0.315
	400	84.9	-85.3%	0.245
	650	82.2	-85.7%	0.605
	900	87.2	-84.9%	0.729
	1150	88.4	-84.7%	0.776
0.0	150	206.6	-64.1%	0.350
	400	84.1	-85.4%	0.236
	650	79.3	-86.2%	0.422
	900	81.2	-85.9%	0.496
	1150	102.3	-82.2%	0.494

TABLE 4.8: Maximum stress, stress reduction, and final volume fraction in a component optimized for 10 MW/m^2 with two different initial distributions.

Using a 14x28-element mesh and a temperature-dependent material model without temperature-dependent sensitivities, iterations required, on average, about 20 - 30 seconds on a notebook computer with a quad-core Intel Core i7.

This permitted simulation of all 20 load cases in one day. Iterations required roughly 100 and 250 seconds when simulating the 10/650 load case with 21x42- and 28x56-element meshes, respectively. For a typical iteration, the sensitivity analysis requires 70 - 75% of the total computation time. Solution of the MMA subproblem requires the bulk of the remaining time, and solution of the thermal and static equilibrium problems amounts to less than 2% of an iteration.

Mesh refinement does not fundamentally change the topology of the material distribution of an optimized component, an issue that is common in traditional topology optimization. Figure 4.12 compares the optimal design for the 10/400 load case on a 14x28- and 21x42-element mesh. Though the average volume fraction and resolution of the solutions differ, the same stress-reducing features develop regardless of element size. Thus, filtering of sensitivities is, in principal, unnecessary. Testing with the weighting function (4.25) further demonstrated that filtering produces virtually no effect. Filtering does increase computational time, however, due to the large number of local constraint functions for which sensitivities must be calculated. The sensitivity filter was therefore not used for the components presented.

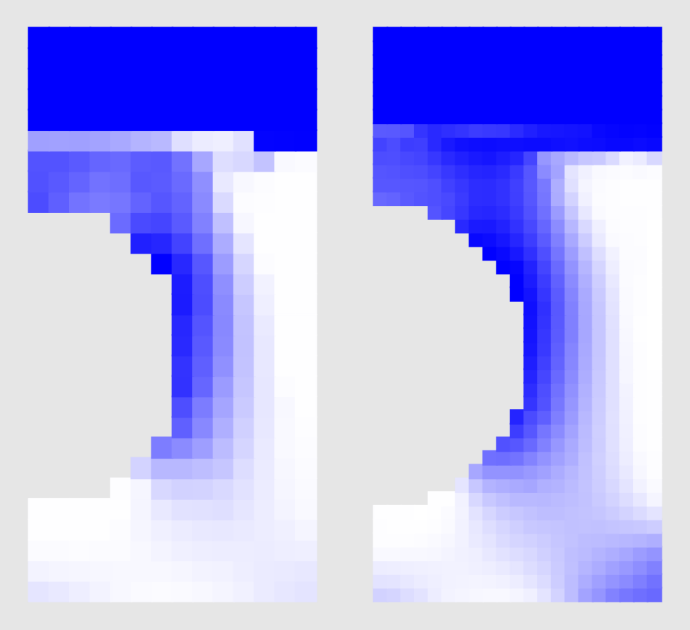

FIGURE 4.12: A BCC component optimized for the 10/400 load case using 14x28- (left) and 21x42-element (right) meshes.

Chapter 5

Sample topology-optimized designs

The following presents two examples of topology-optimized PFC designs. The primary purpose of this chapter is to demonstrate techniques to utilize the output of the topology optimization process to design manufacturable components, and to compare the ability of those techniques to achieve the predicted stress reduction.

The designs presented were compared using the commercial FE software *ANSYS* to simple 2D analyses of traditional components, shown below. The cooling tube was excluded in each model so that the conventional components match the simplified PFC configuration used for the optimized components as closely as possible. Figures 5.1 and 5.2 display, respectively, the domain and stress field in a W monoblock and a W-armored flat-tile design with a CuCrZr heat sink. Each component has an OFHC-copper interlayer. Properties of all three materials were drawn from [64]. The peak von Mises stress was 475.2 MPa in the monoblock, and 517.6 MPa in the flat-tile design.

5.1 Flat-tile mockup with honeycomb

A flat-tile component designed for the 10/400 load case with an optimized honeycomb-reinforced heat sink is pictured in Figure 5.3. The composite's tungsten volume fraction was constrained locally to 0.7. Using the *TopOpt* output as a reference, the design domain was divided in 2D CAD software into four regions with uniform volume fractions of 0.7, 0.45, 0.20, and 0.0. Boundaries between regions are splines drawn manually to visually match the optimal material distribution. Though simplistic, this approach is commonly used to post-process topology-optimized material distributions for mechanically loaded structures. The 2D sketch was imported into *CATIA*, where the region for each intermediate volume fraction was extruded as a separate body. The material

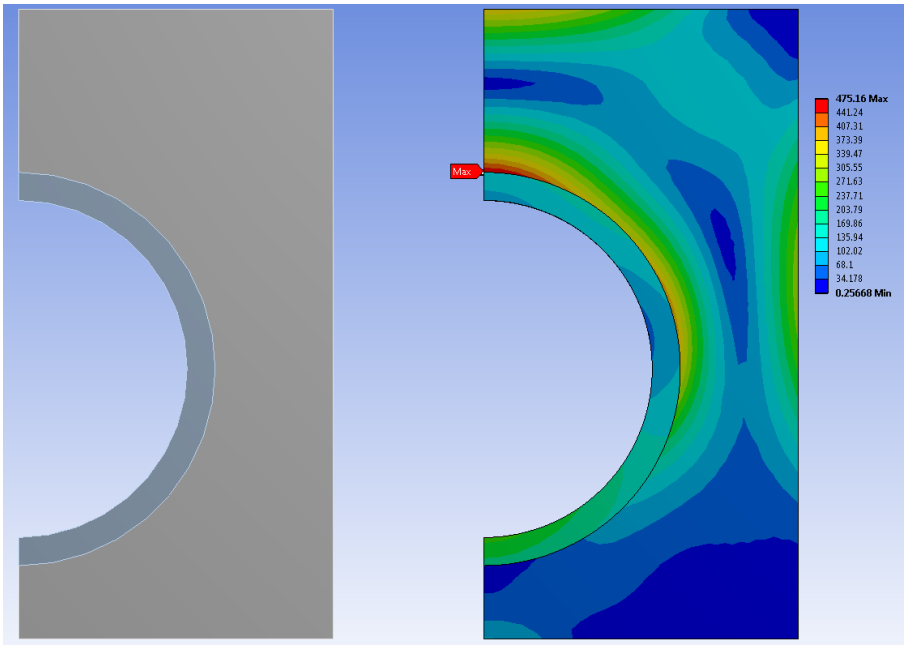

FIGURE 5.1: Two-dimensional model of a traditional monoblock with annular interlayer and the corresponding stress field at 10 MW/m^2. The peak stress is 475.2 MPa.

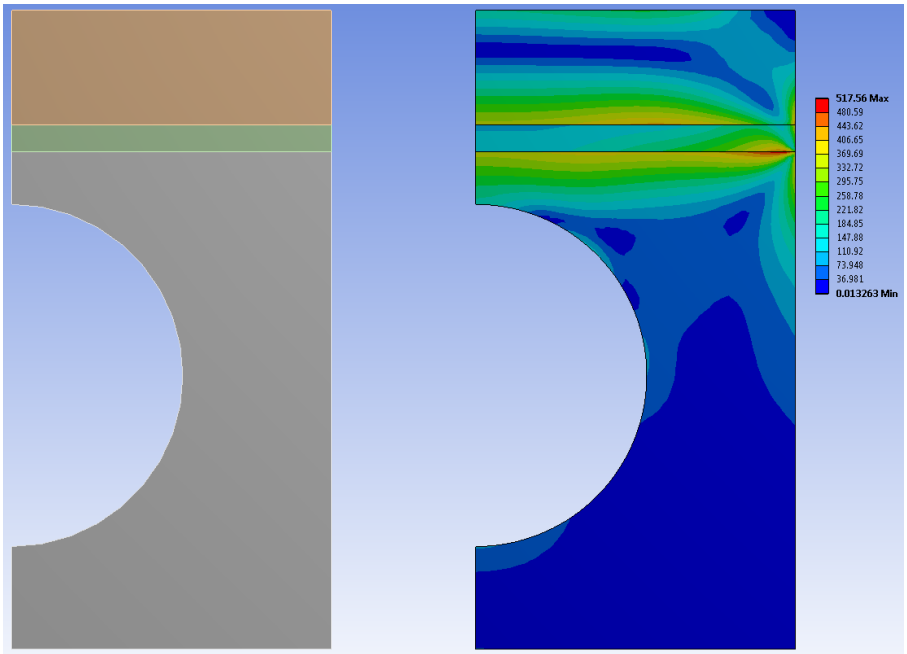

FIGURE 5.2: Two-dimensional model of a traditional flat-tile design with planar interlayer and the corresponding stress field at 10 MW/m^2. The peak stress is 517.6 MPa.

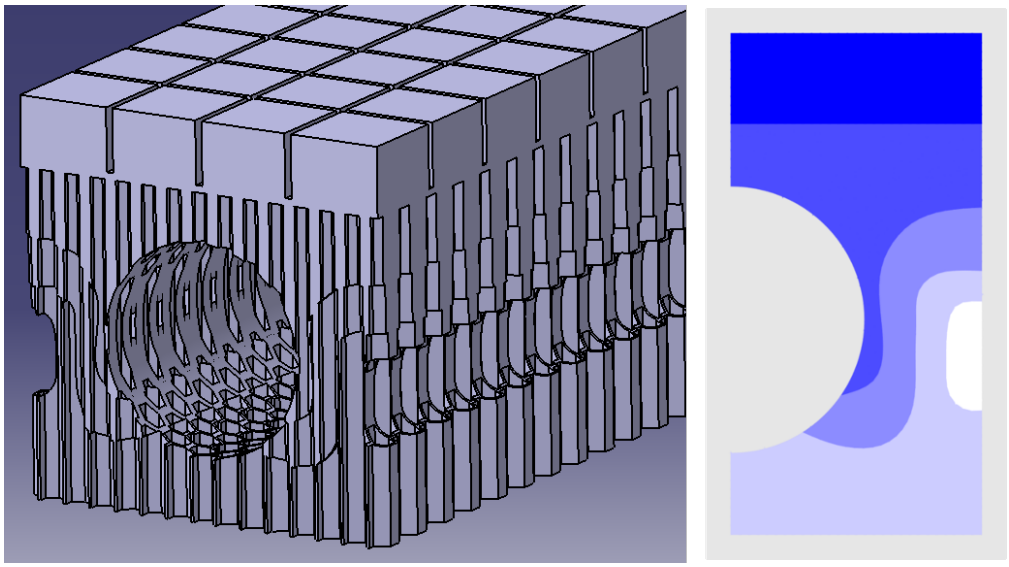

FIGURE 5.3: Post-processed CAD model of a flat-tile design with a honeycomb-reinforced heatsink.

distribution was then realized by intersecting each extruded region with an appropriate uniform honeycomb and subsequently fusing the bodies into one solid.

The optimized component was simulated with a simple 2D FE model in *ANSYS* to verify that the stress reduction predicted during optimization is plausible for a real component (see Figure 5.4). The peak stress in the simulated component is 214.6 MPa. This is a reduction of 54.8% compared to the monoblock model, and 58.5% compared to the flat-tile model. Although this doesn't achieve the predicted stress reduction of approximately 75% (with volume fraction constraint), consider that the reference components in this chapter have the benefit of more realistic modelling and a stress-reducing interlayer. Achieving a 50 - 60% stress reduction with such a simplistic design technique is still a remarkable improvement. This might be further improved with a more refined approach.

5.2 Monoblock tile with BCC lattice

The previous design was post-processed with a simple, manual technique. The optimal material distribution can also be realized with a more systematic method. Figure 5.5 shows a section of a monoblock tile designed with an optimized BCC lattice. The component was optimized for the 10/650 load case with the tungsten volume fraction again constrained to 0.7. Each cell of the lattice is a 2mm cube. The volume fraction in each cell is the average of the

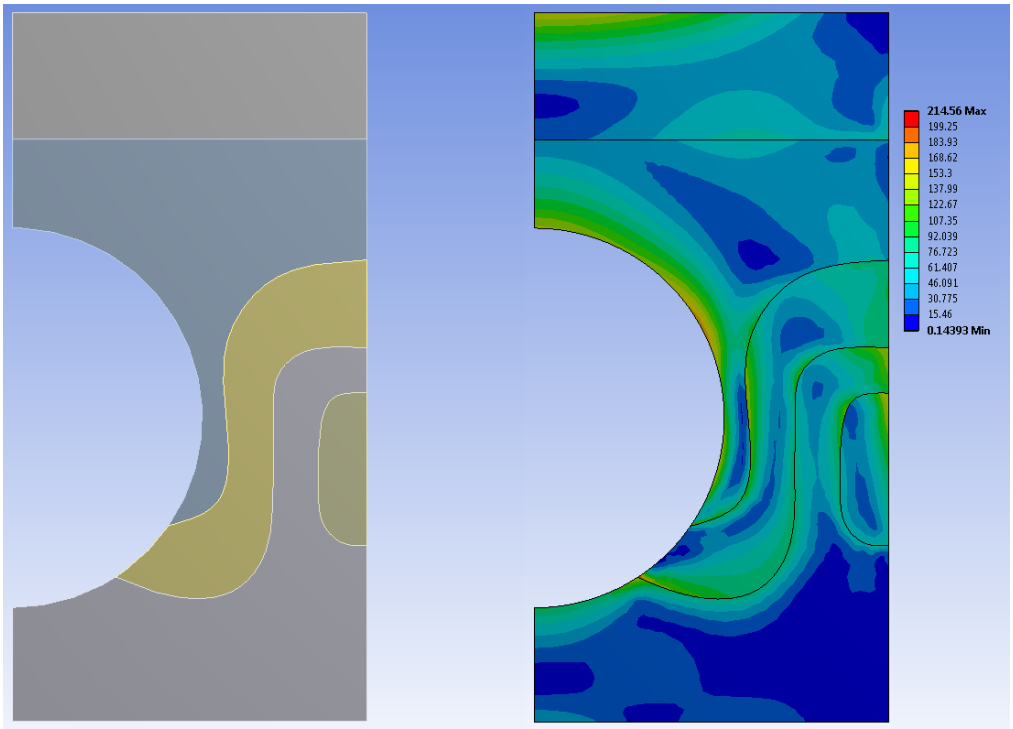

FIGURE 5.4: 2D FE model of the flat-tile design with a honeycomb-reinforced heatsink. The peak von Mises stress is 214.6 MPa.

composition in up to four of the square 1mm elements in the 14x28-element mesh used for the optimization, and was rounded to the nearest tenth (i.e. 0.2, 0.3, etc.). The lattice truss geometry was generated procedurally with the scripting capabilities of *SALOME*. Finishing touches were applied in *CATIA*.

Figure 5.6 shows the *ANSYS* FE model of the optimized BCC monoblock. The peak stress is 207.2 MPa. This is a reduction of 56.4% compared to the monoblock model, and 60.0% compared to the flat-tile model. This method of post-processing showed a minor improvement over the manual technique used for the optimized flat-tile design. Figures 5.4 and 5.6 show that the highest stresses generally occur at the boundaries between regions of different volume fraction. This is a manifestation of the same general problem experienced at any joint between dissimilar materials. The most successful designs will likely be those that 1) capture the optimal material distribution most accurately, and 2) achieve the smoothest transition between regions of different composition.

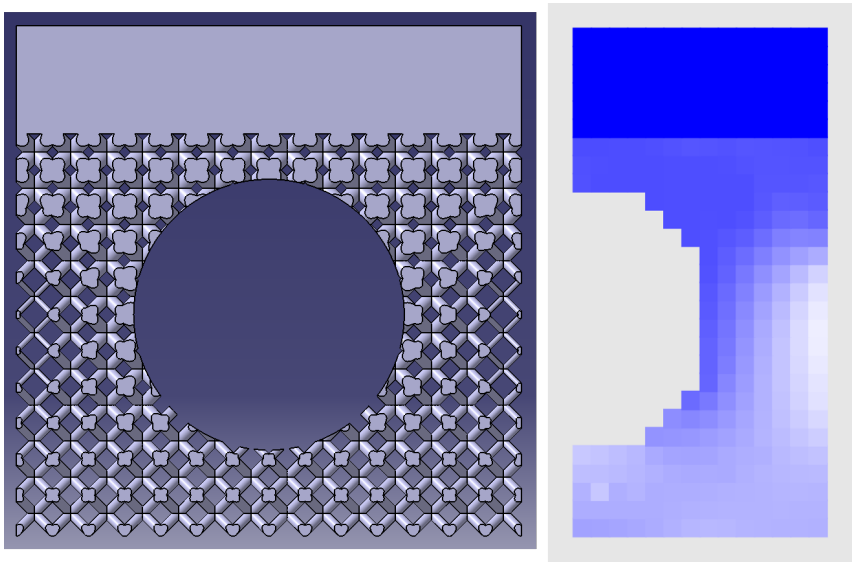

FIGURE 5.5: Monoblock tile designed with an optimized BCC lattice.

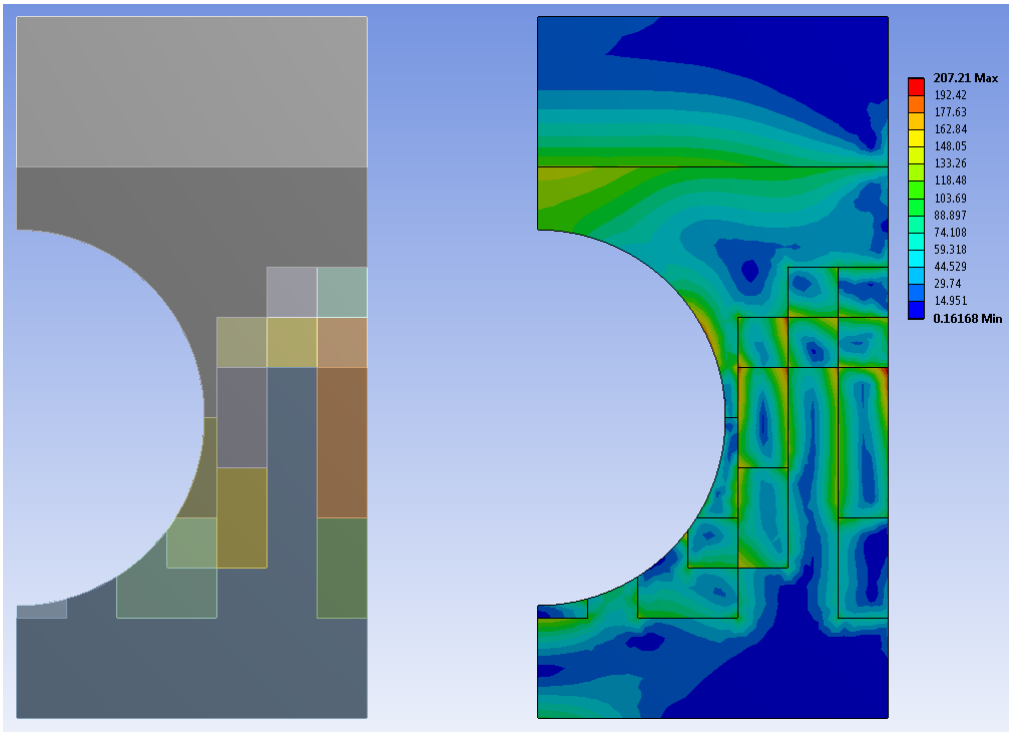

FIGURE 5.6: 2D FE model of the monoblock tile designed with an optimized BCC lattice. The peak von Mises stress is 207.2 MPa.

Chapter 6

Conclusions and outlook

The advantages of AM will soon be available to designers of PFCs. This work has presented a new design methodology that complements the capabilities of AM and promises significant reductions of thermal stress in components exposed to HHF loads. Because melt-infiltrated AM composites are such a recent development, experimental material data is lacking. The homogenization code *homog3d* overcomes this hurdle by predicting the material properties of W_{AM}/Cu composites numerically. The models it produces are essential to optimization techniques using these materials. The *TopOpt* code reduces the stress in PFCs exposed to high heat fluxes remarkably well; the predicted stress reduction reaches 85% in many cases. The final version of this code uses temperature-dependent material properties to provide more realistic results.

The calculation of temperature-dependent sensitivities formally requires the use of total derivatives, which incorporate the dependence of material properties on both the local volume fraction and temperature. However, the contribution of temperature-dependence to the total derivatives of material properties was found to be negligible. Additionally, calculation of total derivatives more than doubles the time required to perform the sensitivity analysis. For these reasons, the suggested approach is to calculate material properties at the current temperature, but to replace total derivatives with partial derivatives with respect to the local design variable. This saves a considerable amount of computation time, and the impact on the solution is inconsequential.

Sample designs were presented demonstrating two ways in which the results of the topology optimization can be used to design components manufacturable with AM. These components exhibit, as predicted, considerably reduced levels of stress compared to traditional PFC designs.

The toolset illustrated in this work is meant as a starting point. The *TopOpt* and *homog3d* codes could be used as presented to design components, given appropriate inputs, but expansion of their capabilities could facilitate better designs: greater stress reduction, improved manufacturability, etc. The ideas

discussed below are potential ways to expand on the methodology that has been presented.

While the optimization problem with local stress constraints reliably yielded good results, the global stress metric didn't achieve the same degree of success. The global formulation shouldn't be completely disregarded, though, because there were cases where it did produce good results. Its speed relative to the local formulation may make further development worthwhile for large problems with numerous design variables. The p-norm is not the only potential stress metric; other metrics could prove more successful. Augmenting the formulation with additional constraints may also improve the feasibility of designs, making them more practical to manufacture.

Optimization tailors a PFC to a specific load case. It was shown that optimized PFCs experience higher stresses at off-nominal conditions. Although the optimized component is still expected to reduce stress compared to traditional designs in most cases, certain combinations of off-nominal conditions can actually lead to poorer performance. Mitigating this issue would make optimized components more versatile. This could potentially be achieved using a multi-objective optimization that minimizes weighted stress values over a range of expected conditions.

As one tends to expect for a structural optimization, the formulation presented exhibits non-convexity; the resulting solutions are known to be local optima. Indeed, examples were presented in Section 4.4 demonstrating the algorithm's failure to reach known better solutions. But the fact that a particular material distribution isn't the best mathematical solution doesn't make it a bad design; realizing stress reductions in the range of 60 - 85% would undoubtedly make components more robust. In addition, there's a practical benefit to finding numerous *good* solutions at the expense of one mathematically *best* solution: this provides the designer with more ways of implementing an optimized component. There are cases, however, where a more thorough solution search would be beneficial; bringing optimized designs with a predicted 60% stress reduction to the 80 - 85% level might be worthwhile. The simplest approach is to perform multiple optimizations, starting with a different initial distribution each time. This is unlikely to be the most robust or efficient approach, however; implementing the globally convergent variant of Svanberg's Method of Moving Asymptotes may yield a more comprehensive search.

Relatively thin components, like monoblocks, are accurately modelled in two dimensions, but designs with significant depth (e.g. long flat-tile components) may benefit from a truly 3D material distribution. Although Section 4.4 only presents results using 2D domains, the *TopOpt* code is generally independent of dimension. Optimization of components in three dimensions is not fundamentally different than in two, but the third dimension does bring new challenges.

Significantly increasing the number of mesh degrees of freedom and design variables causes supralinear growth of memory consumption and calculation times. A faster, more scalable implementation may be necessary to mitigate this effect. In addition to the increased computational expense, visualization of 3D material distributions is not as simple as drawing a single image. Clever visualization of 3D results would aid interpretation and implementation of the optimal structure.

The component-level optimizations performed by *TopOpt* currently use material models with an assumed microstructural topology. Optimization of the microstructure itself is possible as well. This process, known as inverse homogenization, was demonstrated to achieve prescribed elastic properties in [66] and extremal thermal expansion in [54]. As mentioned in Section 2.4, von Müller et al. applied this technique to a 2D W/Cu composite unit cell to minimize the isotropic CTE [43]. An extension of this to three dimensions would be possible by combining elements of *TopOpt* and *homog3d*. Optimizing for other material properties (e.g. thermal conductivity, thermoelastic tensor, non-isotropic behavior) or combinations thereof, could be investigated as well.

Although the inverse homogenization method is effective at producing a microstructure with the desired local properties, a purely microscale treatment neglects the complex interactions that produce stress at the component level. Optimization performed without consideration of these component-level interactions is likely to produce limited results; multi-scale optimization is a more suitable approach. Multi-scale optimization seeks an optimal structural topology at the macro- and microscales concurrently. Examples include Da et al. [67] and Chen et al. [68]. As one would expect for a relatively new branch of topology optimization, initial findings have focused on mechanically loaded structures optimized for minimum compliance; application of the technique to reduce thermoelastic stress would be novel. Current approaches generally assume a uniform microstructure throughout the body. This is a significant restriction for PFCs. Although a uniform microstructure can be used to reduce thermal stress, the results presented in Section 4.4 show that non-uniform material distributions play a major role in stress reduction. This restriction should ideally be avoided, but the alternative – optimization of each microstructural unit cell independently – would generally require tremendous calculation times. The problem lends itself to parallel processing, though; GPU acceleration or cluster computing would make the large number of design variables more manageable.

The tools presented here for optimization of PFCs offer a wealth of design opportunities and a foundation for many future improvements. Topology optimization techniques could be a valuable tool for developing components in the next generation of fusion reactors.

Appendix A

Finite element formulation

This section serves to clarify the details of the FE formulation used for optimization and homogenization simulations. It is meant mainly to introduce an informed reader to the notation used in this work. A full derivation of the finite-element method is available in numerous references.

A.1 Thermal conduction

The temperature field in a PFC is determined by the heat flux received from the plasma, the characteristics of the cooling system, and the conductive properties of the material in between. Temperatures must be recalculated in each iteration of an optimization to account for the changing material distribution. Calculation of a composite's homogenized thermal conductivity also requires solution of a thermal problem. The temperature field T in the body of a composite PFC is governed by the homogeneous form of Poisson's equation with variable thermal conductivity κ:

$$\boldsymbol{\nabla} \cdot (\kappa \, \boldsymbol{\nabla} T) = 0 \tag{A.1}$$

Conventional FE methods were used to convert this continuous partial differential equation into a system of linear equations. Material properties vary throughout the domain. Material composition is considered uniform within an element, but temperature is not. Thus, when the temperature-dependence of properties is considered, unique properties exist at each integration point. The elemental shape function of an element's node i is denoted $N_i^{(e)}$. The temperature within an element e with n_n nodes is then interpolated by

$$T = \sum_{i=1}^{n_n} N_i^{(e)} \, \theta_i^{(e)} = \boldsymbol{N}^{(e)^T} \boldsymbol{\theta}^{(e)} \tag{A.2}$$

The column vectors $\boldsymbol{N}^{(e)}$ and $\boldsymbol{\theta}^{(e)}$ contain the element shape functions and nodal temperatures, respectively. The temperature gradient within an element is derived from the nodal temperatures as

$$\boldsymbol{\nabla} T = (\boldsymbol{\nabla} \boldsymbol{N}^{(e)^T}) \boldsymbol{\theta}^{(e)} = \mathcal{F}^{(e)} \boldsymbol{\theta}^{(e)} \tag{A.3}$$

where the "flux-temperature" matrix $\mathcal{F}$ encapsulates the shape function derivatives:

$$\mathcal{F}_{ij}^{(e)} = \frac{\partial N_j^{(e)}}{\partial x_i} \tag{A.4}$$

Element conductivity matrices are built from $\mathcal{F}^{(e)}$ and the local thermal conductivity tensor by integration over the element volume $\Omega^{(e)}$:

$$\mathcal{K}_t^{(e)} = h_z \int_{\Omega^{(e)}} \mathcal{F}^{(e)^T} \kappa^{(e)} \mathcal{F}^{(e)} \, d\Omega \tag{A.5}$$

Integration is performed with Gauss quadrature. The thickness parameter h_z is constant throughout the mesh for 2D domains and simply set to one for 3D domains. Heat loads are applied to an element by integrating a prescribed heat flux $\hat{\boldsymbol{q}}$ over the element boundary $\Gamma^{(e)}$:

$$\boldsymbol{f}_{\boldsymbol{q}}^{(e)} = -h_z \int_{\Gamma^{(e)}} \boldsymbol{N}^{(e)} \, (\hat{\boldsymbol{q}} \cdot \boldsymbol{n}) \, d\Gamma \tag{A.6}$$

The global conductivity matrix $\mathcal{K}_t$ and heat load vector $\boldsymbol{f}_{\boldsymbol{q}}$ are assembled from their element-level counterparts. The temperature field is then found by solving the global linear system:

$$\mathcal{K}_t \, \boldsymbol{\theta} = \boldsymbol{f}_{\boldsymbol{q}} \tag{A.7}$$

A.2 Static equilibrium

Although no structural loads are applied directly to the simulated PFCs, stresses develop in the body due to non-uniform thermal expansion. These stresses are calculated using the displacements that result from the applied heat load. The system of partial differential equations for static equilibrium takes the form

$$\operatorname{div} \boldsymbol{\sigma} + \hat{\boldsymbol{b}} = \boldsymbol{0} \tag{A.8}$$

Prescribed body loads $\hat{\boldsymbol{b}}$ are not relevant for the simulations in this work. Treatment of this system is simplest when using matrix/vector notation for the elements of the equation. Thus, the elasticity tensor with components E_{ijkl} is represented by the symmetric matrix $\mathcal{C}$. Differentiation is performed with the matrix operator $\mathcal{D}$, with the form

$$\mathcal{D}^T = \begin{bmatrix} \frac{\partial}{\partial x_1} & 0 & \frac{\partial}{\partial x_2} \\ 0 & \frac{\partial}{\partial x_2} & \frac{\partial}{\partial x_1} \end{bmatrix} \tag{A.9}$$

in two dimensions and

$$\mathcal{D}^T = \begin{bmatrix} \frac{\partial}{\partial x_1} & 0 & 0 & 0 & \frac{\partial}{\partial x_3} & \frac{\partial}{\partial x_2} \\ 0 & \frac{\partial}{\partial x_2} & 0 & \frac{\partial}{\partial x_3} & 0 & \frac{\partial}{\partial x_1} \\ 0 & 0 & \frac{\partial}{\partial x_3} & \frac{\partial}{\partial x_2} & \frac{\partial}{\partial x_1} & 0 \end{bmatrix} \tag{A.10}$$

in three dimensions. Stress in the body is proportional to the *mechanical* strain $\boldsymbol{\varepsilon_m}$. This strain is found by removing the contribution of thermal expansion $\boldsymbol{\varepsilon_t}$ from the displacement-derived *actual* strain $\boldsymbol{\varepsilon}$. Stress is calculated as

$$\boldsymbol{\sigma} = \mathcal{C}(\boldsymbol{\varepsilon} - \boldsymbol{\varepsilon_t}) = \mathcal{C}\left(\mathcal{D}\boldsymbol{u} - \boldsymbol{\varepsilon_t}\right) \tag{A.11}$$

The form of the thermal strain $\boldsymbol{\varepsilon_t}$ depends on whether the temperature-dependence of thermal expansion is considered. Assuming no temperature dependence, the thermal strain is simply

$$\boldsymbol{\varepsilon_t} = \boldsymbol{\alpha}\left(T - T_0\right) \tag{A.12}$$

where $\boldsymbol{\alpha}$ is the thermal expansion tensor in vector form. For a 2D, orthotropic material model, $\boldsymbol{\alpha}$ is

$$\boldsymbol{\alpha} = \begin{bmatrix} \alpha_1 & \alpha_2 & 0 \end{bmatrix}^T \tag{A.13}$$

The reference temperature T_0 is an assumed strain-free temperature. When thermal expansion varies with temperature, values are generally tabulated as the *mean* thermal expansion from a common reference (e.g. 20°C). In this case, thermal expansion between two arbitrary temperatures must be calculated with a simulated intermediate step to the common reference:

$$\boldsymbol{\varepsilon_t} = \boldsymbol{\alpha}_T\left(T - 20°\mathrm{C}\right) - \boldsymbol{\alpha}_{T_0}\left(T_0 - 20°\mathrm{C}\right) \tag{A.14}$$

The displacements $\boldsymbol{u}$ are discretized within a 2D element as

$$\boldsymbol{u} = \begin{bmatrix} u \\ v \end{bmatrix} = \begin{bmatrix} \boldsymbol{N}^{(e)^T} & 0 \\ 0 & \boldsymbol{N}^{(e)^T} \end{bmatrix} \begin{bmatrix} d_1^u \\ \cdots \\ d_{n_n}^u \\ d_1^v \\ \cdots \\ d_{n_n}^v \end{bmatrix} = \mathcal{N}^{(e)}\boldsymbol{d}^{(e)} \tag{A.15}$$

This representation can be easily expanded to three dimensions. After discretizing displacement and temperature, the stress field within an element becomes

$$\boldsymbol{\sigma}^{(e)} = \mathcal{C}^{(e)} \left(\mathcal{B}^{(e)} \boldsymbol{d}^{(e)} - \boldsymbol{\alpha}^{(e)} \boldsymbol{N}^{(e)^T} \Delta\boldsymbol{\theta}^{(e)} \right) \tag{A.16}$$

assuming constant thermal expansion. The "strain-displacement" matrix $\mathcal{B}^{(e)}$ relates an element's nodal displacements to the resulting strain field within the element.

$$\mathcal{B}^{(e)} = \mathcal{D}\mathcal{N}^{(e)} \tag{A.17}$$

Conversion of the equations of static equilibrium (A.8) to a linear system is performed in a manner analogous to the thermal system, with the element stiffness matrices

$$\mathcal{K}_s^{(e)} = h_z \int_{\Omega^{(e)}} \mathcal{B}^{(e)^T} \mathcal{C}^{(e)} \, \mathcal{B}^{(e)} \, d\Omega \tag{A.18}$$

and load vectors

$$\boldsymbol{f}^{(e)} = h_z \int_{\Omega^{(e)}} \mathcal{B}^{(e)^T} \mathcal{C}^{(e)} \, \boldsymbol{\varepsilon_t} \, d\Omega \tag{A.19}$$

The assembled global system (A.20) is then solved.

$$\mathcal{K}_s \boldsymbol{d} = \boldsymbol{f} \tag{A.20}$$

With constant thermal expansion, the thermal strain in (A.19) can be expanded and, by removing the discrete temperatures, the integral can be encapsulated into a matrix that maps nodal temperatures to the load vector:

$$\boldsymbol{f}^{(e)} = \left(h_z \int_{\Omega^{(e)}} \mathcal{B}^{(e)^T} \mathcal{C}^{(e)} \, \boldsymbol{\alpha}^{(e)} \, \boldsymbol{N}^{(e)^T} \, d\Omega \right) \Delta\boldsymbol{\theta}^{(e)} = \mathcal{T}^{(e)} \, \Delta\boldsymbol{\theta}^{(e)} \tag{A.21}$$

Bibliography

[1] ITER homepage.

[2] T. Hirai *et al.*, Fusion Engineering and Design **88**, 1798 (2013).

[3] R. Mattas *et al.*, Journal of Nuclear Materials **191-194**, 139 (1992).

[4] G. Federici *et al.*, Journal of Nuclear Materials **283-287**, 110 (2000).

[5] G. Kalinin *et al.*, Journal of Nuclear Materials **283-287**, 10 (2000).

[6] V. Barabash *et al.*, Journal of Nuclear Materials **283-287**, 138 (2000).

[7] R. Neu, Habilitationsschrift, Eberhard Karls Universität Tübingen, 2003.

[8] R. Neu *et al.*, Journal of Nuclear Materials **438**, S34 (2013).

[9] V. Phillips, Journal of Nuclear Materials **415**, S2 (2011).

[10] M. Roedig *et al.*, Fusion Engineering and Design **61-62**, 135 (2002).

[11] Y. Ueda *et al.*, Fusion Engineering and Design **89**, 901 (2014).

[12] S. Fabritsiev, S. Zinkle, and B. Singh, Journal of Nuclear Materials **233-237**, 127 (1996).

[13] G. Kalinin *et al.*, Journal of Nuclear Materials **307-311**, 668 (2002).

[14] E. Visca *et al.*, Fusion Engineering and Design **86**, 1591 (2011).

[15] M. Li, E. Werner, and J.-H. You, Fusion Engineering and Design **89**, 2716 (2014).

[16] C. Linsmeier *et al.*, Nuclear Fusion **57**, (2017).

[17] P. Gavila *et al.*, Fusion Engineering and Design **98-99**, 1305 (2015).

[18] J. You and H. Bolt, Journal of Nuclear Materials **299**, 1 (2001).

[19] J.-H. You, Nuclear Materials and Energy **5**, 7 (2015).

[20] A. v. Müller *et al.*, Fusion Engineering and Design **124**, 455 (2017).

[21] J.-H. You *et al.*, Journal of Nuclear Materials **438**, 1 (2013).

[22] A. Zivelonghi *et al.*, Journal of Nuclear Materials **417**, 536 (2011).

[23] A. Zivelonghi and J.-H. You, Computational Materials Science **84**, 318 (2014).

[24] E. Tejado, A. v. Müller, J.-H. You, and J. Pastor, Journal of Nuclear Materials **498**, 468 (2018).

[25] E. Tejado, A. v. Müller, J.-H. You, and J. Pastor, Materials Science and Engineering: A **712**, 738 (2018).

[26] A. Yan *et al.*, Materials and Design **109**, 79 (2016).

[27] A. Herrmann, H. Greuner, M. Balden, and H. Bolt, Fusion Engineering and Design **86**, 27 (2011).

[28] J.-H. You, Journal of Nuclear Materials **336**, 97 (2005).

[29] H. Greuner, A. Zivelonghi, B. Böswirth, and J.-H. You, Fusion Engineering and Design **98-99**, 1310 (2015).

[30] D. Sun *et al.*, Fusion Engineering and Design **120**, 9 (2017).

[31] I. Gibson, D. Rosen, and B. Stucker, *Additive Manufacturing Technologies*, 2nd ed. (2015).

[32] A. Gebhardt, *Generative Fertigungsverfahren*, 4th ed. (2013).

[33] K. Kempen *et al.*, in *Solid Freeform Fabrication Symposium* (2011), Vol. 22, pp. 484–495.

[34] S. Das, M. Wohlert, J. J. Beaman, and D. L. Bourell, The Journal of The Minerals, Metals, & Materials Society **50**, 17 (1998).

[35] T. Kellner, Airbus gets 1st production jet engines with 3D-printed parts from CFM, 2016.

[36] X. Zhou *et al.*, Journal of Materials Processing Technology **222**, 33 (2015).

[37] D. Wang *et al.*, Applied Sciences **7**, 430 (2017).

[38] A. v. Müller *et al.*, *6th International Conference on Additive Technologies iCAT 2016* (2016).

[39] B. Vrancken, R. Wauthle, J.-P. Kruth, and J. Humbeeck, *24th International SFF Symposium - An Additive Manufacturing Conference, SFF 2013* (2013), pp. 393–407.

[40] B. Vrancken, Ph.D. thesis, KU Leuven, 2013.

[41] R. Bürgel, H. J. Maier, and T. Niendorf, *Handbuch Hochtemperatur-Werkstofftechnik*, 4 ed. (2011).

[42] T. Kurzynowski, I. Smolina, J. Kurzac, and E. Chlebus, *Fraunhofer Direct Digital Manufacturing Conference* (2016).

[43] A. von Müller, R. Neu, U. von Toussaint, and J.-H. You, *DPG-Frühjahrstagung* (2017).

[44] A. Panesar, M. Abdi, D. Hickman, and I. Ashcroft, Additive Manufacturing **19**, 81 (2018).

[45] M. McMillan, M. Jurg, M. Leary, and M. Brandt, Procedia Technology **20**, 178 (2015).

[46] R. Hedayati, M. Sadighi, M. M. Aghdam, and A. A. Zadpoor, Materials **9**, 613 (2016).

[47] B. Hassani and E. Hinton, Computers and Structures **69**, 707 (1998).

[48] O. Sigmund and S. Torquato, Journal of the Mechanics and Physics of Solids **45**, 1037 (1997).

[49] E. Andreassen and C. S. Andreasen, Computational Materials Science **83**, 488 (2014).

[50] B. Hassani and E. Hinton, Computers and Structures **69**, 719 (1998).

[51] H. Baier, C. Seeßelberg, and B. Specht, *Optimierung in der Strukturmechanik*, 2nd ed. (2006).

[52] M. Bendsøe and N. Kikuchi, Computer Methods in Applied Mechanics and Engineering **71**, 197 (1988).

[53] F. Crescenzi *et al.*, Fusion Engineering and Design **98-99**, 1263 (2015).

[54] O. Sigmund, Structural and Multidisciplinary Optimization **33**, 401 (2007).

[55] O. Sigmund and K. Maute, Structural Multidisciplinary Optimization **48**, 1031 (2013).

[56] O. Sigmund, Ph.D. thesis, Technical University of Denmark, 1994.

[57] R. Yang and C. Chen, Structural Optimization **12**, 98 (1996).

[58] P. Duysinx and O. Sigmund, *7th AIAA/USAF/NASA/ISSMO Symposium on Multidisciplinary Analysis and Optimization* (1998).

[59] G. Cheng and X. Guo, Structural Optimization **13**, 258 (1997).

[60] P. Duysinx and M. P. Bendsøe, International Journal for Numerical Methods in Engineering **43**, 1453 (1998).

[61] K. Svanberg, International Journal for Numerical Methods in Engineering **24**, 359 (1987).

[62] K. Svanberg, SIAM Journal of Optimization **12**, 555 (2002).

[63] K. Svanberg, MMA and GCMMA - two methods for nonlinear optimization.

[64] *Appendix A, Materials Design Limit Data*, ITER 222RLN v3.3, 2013.

[65] R. L. Mott, *Machine Elements in Mechanical Design*, 4th ed. (2004).

[66] O. Sigmund, International Journal of Solids and Structures **31**, 2313 (1994).

[67] D. Da, X. Cui, K. Long, and G. Li, Computers and Structures **179**, 1 (2017).

[68] W. Chen, L. Tong, and S. Liu, Computers and Structures **178**, 119 (2017).